PHYSICAL REVIEW APPLIED **21,** 064008 (2024)

Object detection and range finding with quantum states using simple detection

Richard J. Murchie,[*] Jonathan D. Pritchard, and John Jeffers
Department of Physics and SUPA, University of Strathclyde, John Anderson Building, 107 Rottenrow, Glasgow G4 0NG, United Kingdom

(Received 2 August 2023; revised 15 March 2024; accepted 8 May 2024; published 5 June 2024)

The task of sensing the presence of a target object using a weak light source is challenging when the object is embedded in a noisy environment. One possibility is to use quantum illumination to do this, as it can outperform classical illumination in determining the object presence and range. This advantage persists even when both classical and quantum illumination are restricted to identical suboptimal object-detection measurements based on nonsimultaneous, phase-insensitive coincidence counts. Motivated by realistic experimental protocols, we present a theoretical framework for analyzing coincident multishot data with simple detectors. This approach allows for the often-overlooked noncoincidence data to be included, as well as providing a calibration-free threshold for inferring an object's presence and range, enabling a fair comparison between different detection regimes. Our results quantify the advantage of quantum over classical illumination when performing target discrimination in a noisy thermal environment, including estimating the number of shots required to detect a target with a given confidence level.

DOI: 10.1103/PhysRevApplied.21.064008

I. INTRODUCTION

Quantum illumination (QI) describes the process of using a nonclassical light source to perform optical range finding and object detection. The light state is often chosen to be a two-mode squeezed state generated from spontaneous parametric down-conversion (SPDC). It offers an intrinsic advantage over classical illumination (CI) when the emitted signal is weak but there is strong environmental noise [1]. Ideally entanglement in the QI source can be used to obtain up to a 6-dB enhancement over CI via optimal joint measurements [2], however the requirement for phase-sensitive measurements is technically challenging [3–22] or the measurement may not even be known [23,24]. Instead, it is possible to exploit not the entanglement but the strong correlations of the photon pairs generated in the weak limit of the SPDC process to obtain a quantum advantage with a simpler detection protocol. These photon pairs have several possible correlations, including photon number, temporal and spectral. Therefore, in essence, object detection via quantum illumination entails sending a probe state of the light field (conventionally the signal) towards a possible target object and recording the light that reaches the detection system, which may include some signal reflected off the target. The target, if it is present, sits in a noise bath of classical light, which is detected by the signal detector whether or not the target is there. When the the other mode (the idler) is measured, the nonclassical correlations with the signal mode can be used to enhance the sensitivity of the signal mode measurement. An object's presence, for both QI and CI, is revealed by returned signal, otherwise that light is lost to the environment and the object's absence results in a return of solely noise. QI allows us to pick out returned signal photons from this noise more easily and so provides more information per photon sent to the target.

More generally QI (and CI) can be framed as a quantum state discrimination problem, due to the binary situation of the object present (H1) or absent (H0) hypotheses [25]. It is well known that illumination with an entangled source can improve the distinguishability between two returned quantum states, even in entanglement-breaking conditions [26]. Furthermore, while not optimal, analysis of systems with independent quadrature measurements on the signal and idler show that QI retains an advantage over CI, while not necessarily being better than the best possible classical source [27–29]. Analysis from another approach for QI with independent quadrature measurements, which uses heterodyne measurement on the signal channel to condition the idler channel with a phase shift for the idler-channel homodyne measurement, demonstrates a 3-dB enhancement in the error-probability exponent compared to the optimal classical system [30–32]. Furthermore, it

---

[*] Corresponding author: richard.murchie@strath.ac.uk

has been shown that QI with photon counting and second-order correlation measurements retains advantage over CI [33–38]. Recently, a QI-based target-detection method using nonlocal cancelation of dispersion has been developed [39,40]. More pertinently however, QI with simple photocounting by click detectors has also been shown to provide a quantum enhancement [41–47]. A protocol for achieving Heisenberg-limited velocity estimation using photon counting based on the Doppler effect has also been developed [48,49]. The quantum advantage of QI with simple photocounting by click detectors is smaller than the previously discussed enhancements because such simple detection is suboptimal in the sense that it does not saturate the Helstrom bound and so reveals less information about the quantum state than ideal measurement would [50]. However, QI with photon counting using click detectors is the easiest to implement experimentally, which suggests that it is suitable as an approach for developing a practical quantum-enhanced LIDAR.

Object detection and range finding in a realistic noise and loss environment is challenging. A heralded quantum illumination scheme can provide signal states to interrogate the object that are very different, depending on the result of the heralding measurement, which provides a quantum advantage. However, as we shall see, with noise and loss this quantum advantage disappears almost completely by the time the light gets to the detectors. We show that the detectors themselves result in suboptimal measurements, all of which means that we need a framework that can work with the tiny remaining advantage over multiple experimental shots. This paper presents such a model for object detection and range finding with quantum states using simple detection with Geiger-mode click photodetectors. While range finding in a QI-based detection scheme has been demonstrated before [51–54], the method that we present treats detector data differently in that multiple detector data channels are condensed into a single metric. This approach means the often-overlooked information from noncoincidence events can also be included to enhance state discrimination. The method facilitates comparison between different detection schemes, for example, CI and QI, for inference of an object's presence and range via a metric whose interpretation depends on the likelihood of an object's presence. Our results quantify the advantage of quantum over classical illumination when performing target discrimination in a noisy thermal environment. We provide an operator-friendly approach to quantifying system performance via estimation of the time required to detect a target with a given confidence level. Our experimentally motivated theoretical framework has been applied to demonstrate the jamming resilience of quantum range finding [55].

The paper is organized as follows. In Sec. II an overview of the model system for CI and QI is given. It provides a description of the heralding effect that QI exploits and why, after interaction with the target, this effect is tiny. This provides a justification for our model. Section III describes object detection without timing information, detailing quantum hypothesis testing and the log-likelihood value (LLV) framework for interpreting detector data. We compare it with more familiar state distinguishability error bounds to give a comparison with the best possible measurement scheme. We also compare our scheme with a classical illumination scheme that uses the same Geiger-mode detectors and show that there is a significant quantum advantage. In Sec. IV we explore the effect of target distance on the object-detection protocol. Section IV B describes the range-finding protocol, incorporating expected delay and click stream matching. Finally, Sec. V provides a discussion and outlook.

II. SYSTEM OVERVIEW

A. Schematic of classical and quantum illumination

An overview of the system for performing optical detection of a target object immersed in a thermal background using simple detection is shown schematically in Fig. 1 for both classical and quantum illumination regimes. For the CI case, a thermal beam is used to interrogate the target and data provided by recording click counts on the signal detector. We consider a QI source produced by a pulsed pump laser with repetition rate f_{rep}. Each pump pulse produces, via parametric down-conversion [56,57], a QI source state located centrally within a single-pulse temporal window of duration $1/f_{\text{rep}}$. The mechanism for state production is a close-to simultaneous photon pair production from one pump photon. The quasisimultaneous nature of the pair production provides effective short-term temporal correlations that are exploited to enable target detection and range finding via coincident detection. Outside this very short timescale the two beams are effectively uncorrelated. Each state is described mathematically by the two-mode squeezed vacuum state (TMSV), and we assume that the pump is of a strength that it produces a TMSV with a mean photon number much smaller than one. This state is distributed over two spatially separated modes: the signal beam and the idler beam. Within the short correlation timescale the TMSV has nonclassical photon-number interbeam correlations; outside it the two beams are uncorrelated. Note that for QI we do not necessarily require a pulsed pump. The intrinsic correlations of the SPDC source enable this same framework to be applied to a cw pump with the corresponding time window of a single shot equal to a coincidence detection window duration τ_c. Note that there are other nonclassical correlations in the SPDC output that could be exploited, such as spectral correlations [52], or polarization, but we do not use these in this work.

For CI we assume that the signal is a pulsed thermal source with repetition rate f_{rep}, but filtered to have the the

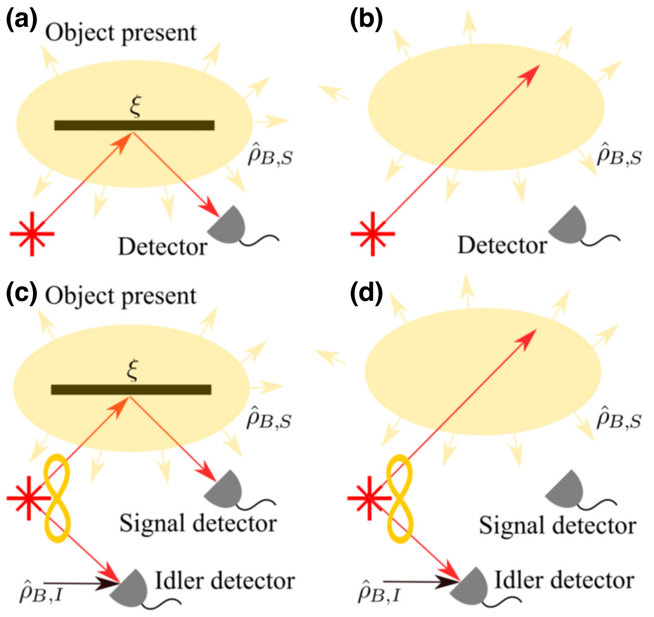

FIG. 1. Schematic of optical LIDAR for a target of finite reflectivity ξ in a thermal background $\hat{\rho}_{\mathrm{B,S}}$. In the CI regime with target (a) present or (b) absent, a thermal signal beam is used to interrogate the target with a single signal detector used to measure the return field mode. In the QI regime with target (c) present or (d) absent, a photon pair source is used to illuminate the target, with an additional detector used to directly measure the idler mode (accounting for idler background noise $\hat{\rho}_{B,I}$) providing a coincident detection channel.

same frequency and mean photon number as the signal. We use its statistics to derive the single-shot click probabilities associated with a single-pulse window duration $1/f_{\mathrm{rep}}$. Such a modulated temporal reference is essential for performing range finding in the classical system.

The detectors assumed by our model are Geiger-mode avalanche photodiodes, insensitive to phase and which register a click or a no-click event for each experimental shot of the system, hence the term "simple detection" [58]. As the signal is produced near the single-photon level the detectors are thresholded such that they can be triggered by single-photon events. This makes them appropriate for use in realistic low-signal strength-sensing environments.

Losses incurred during the full target identification process are included in the model. Both system loss (includes detector quantum efficiency) and signal attenuation from the process of probing a target object are modeled by beam-splitter transformations [59,60]. The two input states of the beam splitter are the background noise (or, for a detector, the source of dark counts) and the probe-mode signal state. Therefore, the two beam-splitter output states are the reflected mode destined for the detector and a traced-out mode, which is discarded. This partially traced beam-splitter transformation facilitates the mixing of signal and noise, while also modeling signal loss. The mathematical beam-splitter models for QI and CI are illustrated in Fig. 2. It is valid to think of CI with single-photon detectors and low mean photon numbers as a quantum scheme. When a detector fires it measures something very close to a single-photon state. However, we make the distinction that the overall statistics of the counts will not be nonclassical, hence CI, while recognizing that this is a choice with a degree of arbitrariness. For QI the difference photon statistics are nonclassical.

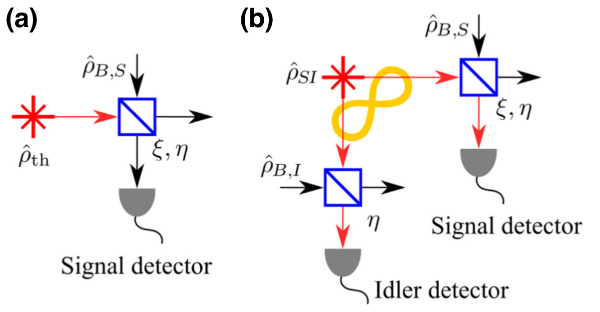

FIG. 2. Simplified detection model using beam-splitter transformations. (a) In the CI regime a beam splitter is used to mix the thermal signal beam ρ_{th} with the thermal background $\hat{\rho}_{\mathrm{B,S}}$ using parameters ξ and η to account for finite target reflectivity when the object is present and system loss. (b) For QI the light source is a two-mode correlated thermal state $\hat{\rho}_{SI}$, with a second beam splitter in the idler path to account for idler background noise $\hat{\rho}_{B,I}$ and system loss η.

B. Quantum state descriptions

There are two easily produced signal states typically considered for CI, the single-mode thermal state and the single-mode coherent state [61]. The density matrix for the single-mode thermal state is

$$\hat{\rho}_{\mathrm{th}} = \frac{1}{\bar{n}+1}\sum_{n=0}^{\infty}\left(\frac{\bar{n}}{\bar{n}+1}\right)^{n}|n\rangle\langle n|, \tag{1}$$

where $\bar{n}$ is the mean photon number of the state and $|n\rangle$ is a photon-number state in the relevant mode. The thermal state has no off-diagonal density-matrix elements. This is not true for the coherent state, which is characterized by a complex number α.

If we write the coherent state in density operator form and disregard the off-diagonal elements

$$\hat{\rho}_{\mathrm{coh}} = e^{-|\alpha|^2}\sum_{n=0}^{\infty}\frac{|\alpha|^2}{n!}|n\rangle\langle n|. \tag{2}$$

This is valid as the detectors are insensitive to off-diagonal elements of the density matrix. This state has Poissonian photon statistics, compared with the superpoissonian photon statistics of the thermal state, which causes the coherent state to perform slightly better than the thermal state at target detection, at the expense of a little covertness. This relative reduction in covertness occurs because an intruder could measure the second-order correlation function $g^2(0)$ of the coherent state, which is distinct from that of the thermal background. Furthermore, its spectral linewidth will probably be far smaller than the background noise, which is intrinsically multimode. Throughout this paper only the single-mode thermal state for CI will be considered in the results and discussion. Consideration of CI as a protocol allows for performance comparison relative to QI, in order to seek out a quantum advantage. Despite the fact that the CI presented here is not at its full potential due to the exclusion of the coherent state, the differences in results presented are small in the low mean photon-number regime.

The state used in the QI simple detection system is a two-mode squeezed vacuum (TMSV),

$$|\psi\rangle = \frac{1}{\sqrt{\bar{n}+1}} \sum_{n=0}^{\infty} \left(-e^{i\theta} \sqrt{\frac{\bar{n}}{\bar{n}+1}} \right)^n |n, n\rangle, \qquad (3)$$

where the first and second components of the state are, respectively, the signal and idler photon number, which are constrained to be identical. The quantum theory of generating the TMSV is based on using a strong pulsed coherent pump field driving a nonlinear material, as described in Sec. II A. This causes spontaneous parametric down-conversion, which results in the TMSV. The density matrix of the signal and idler modes is simply the projector based on this state,

$$\hat{\rho}_{SI} = |\psi\rangle\langle\psi|, \qquad (4)$$

where S and I denote the signal and idler mode, respectively. However, our detectors are insensitive to off-diagonal elements of this state so we could disregard them with no detriment to our calculations, effectively providing the two-mode correlated thermal state

$$\hat{\rho}_{SI} = \frac{1}{\bar{n}+1} \sum_{n=0}^{\infty} \left(\frac{\bar{n}}{\bar{n}+1} \right)^n |n\rangle_I\langle n| \otimes |n\rangle_S\langle n|. \qquad (5)$$

In any case, the state has nonclassical photon-number correlations and approximates the real state for an appropriate correlation timescale. The mean photon number depends on the second-order nonlinearity of the material $\chi^{(2)}$ and the pump-field mean photon number [62]. If we trace over the idler mode, the signal light $\hat{\rho}_{SI}$ has the unconditioned measurable properties of a single-mode thermal state. This facilitates covertness as an intruder who does not have access to the idler beam is ill poised to identify this state as it has the photon-number statistics and coherence of the same form as a weak thermal background [52]. This tracing of the QI state reduces it to a single-mode CI state and means that QI will always perform better than this state. The purpose of CI in this paper is to provide the means for a quantum advantage to be quantified, for the two protocols that use the same amount of light directed towards a possible target and which are practical for implementation outside of laboratory environments.

The background-noise system is modeled by a single-mode thermal state. We will assume that the thermal state has the same spectral properties of the signal state, or that we can spectrally filter it to do so. The CI and the QI signal detector dark counts are assumed thermal with a mean photon number $\bar{n}_{B,S}$. The QI idler detector dark counts background noise has a mean photon number $\bar{n}_{B,I}$.

C. Detector modeling and measurements

The detectors register, for a single experimental shot, either a click or a no-click event. The probability of a click event, which is the expectation value of the product of the signal state and the click event measurement operator, or positive operator-valued measure (POVM) element [63], is calculated. An increase in mean photon number incident on the detector raises the probability of a click event. The no-click POVM element is denoted $\hat{\pi}_\times$ and the click event POVM element $\hat{\pi}_\checkmark = \hat{1} - \hat{\pi}_\times$. Beam-splitter transformations and tracing out of unobserved modes, as in Fig. 2 provide the POVM elements, as derived in Appendix A, where Eq. (A12) defines the generic click POVM element. In this simplified treatment, the deleterious effects of detector dead time, after pulsing, and timing jitter are assumed negligible due to the performance of technology available and the low mean photon numbers considered. Their effects are relatively simple to include, but complicate the theory. Then the signal detector click POVM element is

$$\hat{\pi}_S = \hat{1} - \frac{1}{1+\bar{n}_{B,S}} \sum_{n=0}^{\infty} \left(1 - \frac{\eta_S \xi}{1+\bar{n}_{B,S}} \right)^n |n\rangle\langle n|, \qquad (6)$$

where $0 \leq \xi \leq 1$ is the signal attenuation factor, which accounts for all loss from the process of probing a target. When denoting a POVM element the ✓ subscript has been suppressed, and will be for the rest of the paper. The system loss parameter in the signal detector channel is signified by η_S, where $0 \leq \eta_S \leq 1$, and includes detector quantum efficiency and coupling losses, for example. The signal detector background noise $\bar{n}_{B,S}$ is included in the POVM element too. The inclusion of noise and inefficiencies causes the effect of click measurement to effect the projection of the state onto a mixed state, the complement of a probability-weighted thermal state rather than onto the complement of the vacuum.

In line with the above, the CI object present click probability is

$$\mathrm{Pr}_{\mathrm{H1:CI}} = \mathrm{Tr}\big(\hat{\pi}_S \hat{\rho}_{\mathrm{th}}\big). \qquad (7)$$

On the other hand, if the target is absent, the signal state at the detector is the environment state, which is strictly a thermal state. In our model this is included in the detector POVM element, so the signal state at the detector becomes the single-mode vacuum, as the signal is lost to the environment. Therefore for CI, the click probability when the target is absent is

$$\mathrm{Pr}_{\mathrm{H0:CI}} = \mathrm{Tr}\big(\hat{\pi}_S|0\rangle\langle 0|\big). \tag{8}$$

For QI there is another detector, the idler, which has its own POVM element. The idler POVM element is

$$\hat{\pi}_I = \hat{1} - \frac{1}{1+\bar{n}_{B,I}} \sum_{n=0}^{\infty} \left(1 - \frac{\eta_I}{1+\bar{n}_{B,I}}\right)^n |n\rangle\langle n|. \tag{9}$$

This POVM element includes the system loss of the idler detector channel η_I and the measured idler detector background noise $\bar{n}_{B,I}$.

The probability of an idler-click event is

$$\mathrm{Pr}_I = \mathrm{Tr}\big(\hat{\pi}_I \hat{\rho}_{SI}\big). \tag{10}$$

Such a click event on the idler detector conditions the signal state, which is then measured by the signal detector. In a noiseless and perfect efficiency system this conditioning heralds the presence of at least one photon in the signal mode, as measurement of an idler click conditions the signal state to have a mean photon number of $\bar{n}+1$. This conditioning also shows that the heralding gain, $1+1/\bar{n}$, is largest when $\bar{n} \ll 1$, such that a single signal photon is produced by an idler click. The reason for this is clear if we examine the photon-number probability distributions of the conditioned states. If the idler detector does not fire the photon-number probability distribution of the signal is conditioned to be the vacuum state. If the idler fires the signal state becomes a thermal distribution shifted upwards by one photon. This is illustrated in Fig. 3(a), which shows the photon-number distributions of the unconditioned state $\hat{\rho}_S$, the idler-click conditioned state $\hat{\rho}_{S|I,1}$ and the idler no-click conditioned state $\hat{\rho}_{S|I,0}$, all incident upon the signal detector in the case of no noise and no system loss. The two states have disjoint photon number distributions. There would be some overlap between the two conditioned distributions if the idler detector did not have unit quantum efficiency, but they would still be clearly different.

In a more realistic quantum LIDAR scenario, however, noise, system loss and high signal attenuation cause the conditioned signal photon-number distributions to become much less clear cut in their differences. Figure 3(b) illustrates this. For the parameters shown the unconditioned, no-click conditioned, and click-conditioned signal photon-number distributions are hardly different. We can see the size of the conditioning effect if we take the difference in the two conditioned probability distributions, $\Delta P(n) = P(n)_{I,1} - P(n)_{I,0}$, which is plotted as an inset. This difference shows the small residual conditioning effect. It is clear from Fig. 3 that the effect of an idler click is to suppress (or reduce) the vacuum contribution in the conditioned state incident upon the signal detector. Appendix B provides a derivation of the photon-number distributions in Fig. 3(b). It seems clear that conditioning in a realistic system with multiple shots of the experiment will cause only a tiny change in the number of counts at the signal detector when the idler fires. Hence a well-developed statistical framework is required to extract the information. It should also be noted that the parameters used in Fig. 3(b) understate the difficulty when using realistic parameters encountered experimentally. Of course, most detectors are not photon-number resolving, so it is not possible to use all of the information from the photon-number distributions, adding further credence to the demand for a powerful statistical framework.

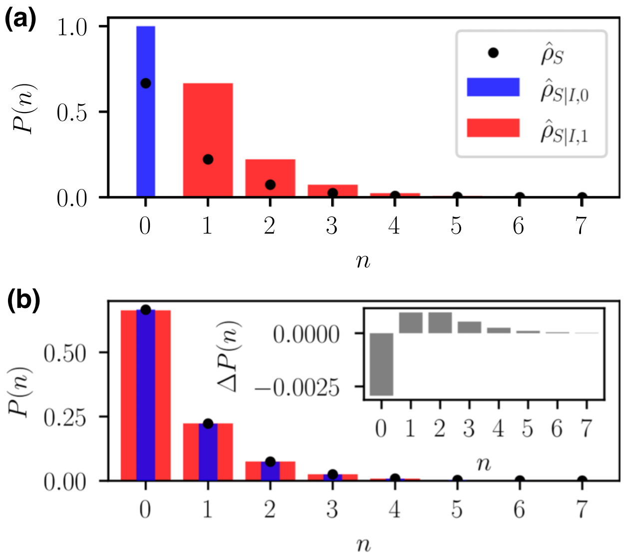

FIG. 3. Photon-number distributions in the case of no noise or loss and perfect detection (a) and the case with noise, system loss, and signal attenuation (b). Plotted are the unconditioned state (black dots), idler-click conditioned state (orange bars), and idler no-click conditioned state (thin blue bars). Inset in (b), the difference of the idler conditioned states' photon-number distributions $\Delta P(n)$. Mean photon number of the signal state $\bar{n} = 0.5$, system loss of all detectors $\eta_{S/I} = 0.5$, signal attenuation factor $\xi = 8.84 \times 10^{-3}$, mean photon number of background and dark counts for signal detector $\bar{n}_{B,S} = 0.5$, and mean photon number of background and dark counts for idler detector $\bar{n}_{B,I} = 4.49 \times 10^{-4}$.

There are two possible types of click events for the signal detector, the coincidence click and noncoincidence click. The probability of a coincidence click and noncoincidence click (or alternatively the probability of a signal click given an idler click or no click) when an object is present, are, respectively,

$$\mathrm{Pr}_{S|I,1} = \mathrm{Tr}\left(\hat{\pi}_S \frac{\mathrm{Tr}_I(\hat{\pi}_I \hat{\rho}_{SI})}{\mathrm{Pr}_I}\right), \tag{11}$$

$$\mathrm{Pr}_{S|I,0} = \mathrm{Tr}\left(\hat{\pi}_S \frac{\mathrm{Tr}_I((\hat{1} - \hat{\pi}_I)\hat{\rho}_{SI})}{1 - \mathrm{Pr}_I}\right). \tag{12}$$

The object-absent click probabilities for QI are now described. The idler-click probability Pr_I is not affected by the object and the coincidence and noncoincidence probabilities are now both equivalent to

$$\mathrm{Pr}_{\mathrm{H0}} \equiv \mathrm{Pr}_{\mathrm{H0:CI}}. \tag{13}$$

These probabilities underpin the theory for target object detection.

III. OBJECT DETECTION

A single-shot measurement with simple click detectors cannot effectively distinguish between the two cases of object present and absent. This is because when background noise is present a click in a single-shot system can either originate from the reflected signal beam or from background noise. Hence, multishot quantum hypothesis testing is required [64–67].

Each shot of the experiment at each detector corresponds to a Bernoulli trial. A click or no-click event occurs according to a click probability and generates a corresponding binomial click-count distribution [68]. In order to infer an object's presence or absence, comparison of the relevant click-probability distributions is required [69]. In the limit of many shots, the binomial click distributions can be approximated as Gaussian, under the assumption that the criterion detailed in Appendix C is satisfied. This valid approximation greatly simplifies the analysis and computational demands and is used henceforth.

Each set of system parameters gives rise to an idler-click distribution P_I, and each value in P_I has a corresponding object present P_{H1} and absent P_{H0} signal click distribution. Figure 4 shows the coincidence and noncoincidence click distributions for both object present and absent cases, after a set number of idler-click events $k = 1.98 \times 10^4$.

Existing literature often overlooks noncoincidence signal clicks events as a source of useful information. Equation (25) quantifies the advantage provided by the inclusion of noncoincidence clicks, followed by a discussion of the regimes where this advantage is more pronounced. In addition, the recording of all types of clicks is required for the range-finding protocol discussed later in this paper. The rest of this paper will focus on QI as it is straightforward to reduce the QI theory to CI only. The protocol is explained without CI explicitly mentioned unless a performance comparison between CI and QI is made.

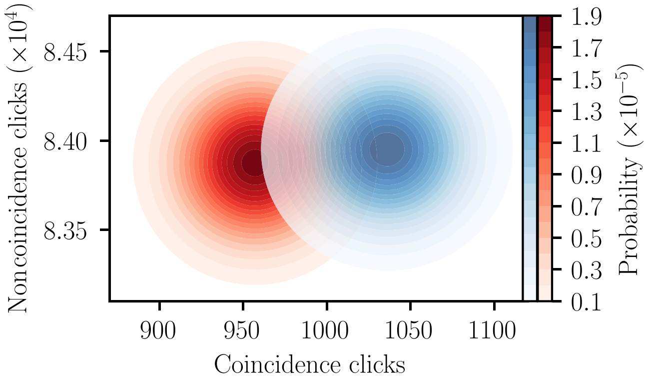

FIG. 4. Quantum illumination probability distribution displaying coincidence click counts and noncoincidence click counts for both object present (colored blue) and absent (colored red) cases. Mean photon number of the signal state $\bar{n} = 2.19 \times 10^{-2}$, system loss of all detectors $\eta_{S/I} = 0.5$, signal attenuation factor $\xi = 8.84 \times 10^{-3}$, mean photon number of background and dark counts for signal detector $\bar{n}_{B,S} = 5.06 \times 10^{-2}$, and mean photon number of background and dark counts for idler detector $\bar{n}_{B,I} = 4.49 \times 10^{-4}$. The number of shots is 1.76×10^6 and the number of idler-click events displayed is 1.98×10^4.

The make up of a shot is a topic that has been already considered briefly in Sec. II A. Our model assumes a perfect one-to-one mapping of pulses to shots (with a repetition rate set by f_{rep}). This is perfectly fine in the low detector timing jitter regime and where count rates are slow enough that detector dead times are negligible. While it is easy to set the temporal duration of a shot for a pulsed source, as the reciprocal of the source repetition rate, it is not the case for cw systems, which require f_{rep} to be artificially set through the choice of the coincidence window duration $f_{\mathrm{rep}} = 1/\tau_c$. However, the second-order coherence function $g^2(\tau)$ can instruct what temporal duration for a shot is sensible, for both cw and pulsed. Due to the spontaneous and stimulated aspects of the nonlinear process there could be many modes within one shot temporal window size, however it suffices to model each shot to only have one mode of the source due to the nature of the detectors and the low mean photon number. As such, the click probabilities are easily found via the method presented earlier. It is clear that the mean photon numbers for the source and background are dependent on the temporal window size of a shot. Henceforth this paper focuses on a pulsed pump source, noting that extension to idler-detector-gated cw is relatively straightforward.

A. Log-likelihood value

A click-count value might infer an object's presence in one parameter regime or an object's absence in another. Hence, a framework is desired that allows for fair comparison of incoming click data between different situations. The log-likelihood value (LLV) forms the basis of this framework. The LLV is also appropriate for use in dealing with multichannel detector data, as it reduces multiple channels of data pertaining to two simple hypotheses into a single value. This value also provides a simple test, in this context commonly known as the likelihood ratio test. The use of the LLV for hypothesis testing is justified by the Neyman-Pearson lemma, which states that it provides the most powerful test for a set statistical significance level [70].

The object present P_{H1} and absent P_{H0} click distributions in their binomial form after N shots and k idler-click events define the LLV after k idler clicks, which converts click data $\underline{x}$ into a LLV

$$\Lambda(\underline{x}, k) = \ln\left(\frac{P_{\mathrm{H1}}(\underline{x}, k)}{P_{\mathrm{H0}}(\underline{x}, k)}\right), \tag{14}$$

where $\underline{x} = (x, y)$ with x the coincidence click count and y the noncoincidence click count. It can be seen from the definition that $\Lambda(\underline{x}, k) > 0$ means that an object's presence is more likely, that $\Lambda(\underline{x}, k) = 0$ means that both regimes are equally as likely, and $\Lambda(\underline{x}, k) < 0$ infers that an object's absence is more likely. An advantage of using the LLV as a test is that it can be self-calibrating to a LLV detection threshold $d_{\mathrm{LLV}} = 0$, as the detection decision will automatically be set according to the likelihood of an object's presence. We will consider later in Sec. III C the effect of setting LLV decision levels on false-alarm probabilities and their extension to receiver operator curves.

As the click probabilities, click data, and number of shots are all real and positive Eq. (14) can be stated as a linear equation

$$\Lambda(\underline{x}, k) = (M_1 x + kC_1) + (M_2 y + (N - k)C_2). \tag{15}$$

In Appendix D this transformation is formulated in linear equation form and constants M_1, M_2, C_1, C_2 are defined.

We express the statistical moments of the LLV distributions when there has been a mean number of idler clicks $k = \mu_I = N\mathrm{Pr}_I$ in the following analysis. The object present $P_{\mathrm{H1}:\Lambda(x,\mu_I)}$ and absent $P_{\mathrm{H0}:\Lambda(x,\mu_I)}$ LLV distributions for idler clicks $k = \mu_I$ are shown in Fig. 5. For our analytic treatment of the LLV distributions, we condition solely off the mean number of idler clicks μ_I, which is reasonable as the standard deviation of the number of idler clicks σ_I is sufficiently small compared to the mean μ_I. For the parameters in Fig. 5 the variance in the number of idler clicks is $\sigma_I^2 = 1.96 \times 10^4$. As the click-count distributions originate from a binomial distribution, the variance is always less than the mean, which ensures that conditioning off the number of expected idler clicks is appropriate. Furthermore, the click-count distributions differ from the photon-number distributions as they do not infer the photon statistics of the state of light in question. Assuming that the click distributions are well approximated by a Gaussian, all of the LLV distributions are Gaussian too, as linear transformations and combinations preserve normality [71]. The reason for the discrepancy of the maximal value between the object present and absent LLV distribution in Fig. 5 is due to the object present distribution having a larger variance for these parameters. The difference of variance, if there is any, is in that the idler-click conditioned click events affect the signal click-probability distribution, whereas the idler clicks are decoupled from the signal click-probability distribution when there is no target. The results below show the object present case, but the analysis is similar for object absent. The mean and standard deviation for the object present LLV distribution after mean idler clicks as derived in Appendix E is

$$\begin{aligned}\mu_{\mathrm{H1}:\Lambda(x,\mu_I)} &= N\big(\mathrm{Pr}_I(M_1\mathrm{Pr}_{S|I,1} + C_1 - M_2\mathrm{Pr}_{S|I,0} - C_2) \\ &\quad + M_2\mathrm{Pr}_{S|I,0} + C_2\big), \qquad (16)\\ \sigma_{\mathrm{H1}:\Lambda(x,\mu_I)} &= \big(N(\mathrm{Pr}_I(M_1^2\mathrm{Pr}_{S|I,1}(1 - \mathrm{Pr}_{S|I,1}) \\ &\quad - M_2^2\mathrm{Pr}_{S|I,0}(1 - \mathrm{Pr}_{S|I,0})) \\ &\quad + M_2^2\mathrm{Pr}_{S|I,0}(1 - \mathrm{Pr}_{S|I,0})\big)^{0.5}. \qquad (17)\end{aligned}$$

The LLV framework is used to discriminate between the presence or absence of an object, hence it is worthwhile to compare the performance of this method to optimal discrimination set by the Helstrom bound [50]. The Helstrom bound does not provide the experimental detection scheme that would perform the optimal discrimination, but reveals the optimum POVM, which ensures the minimum probability of error. A single-shot click measurement does not saturate the Helstrom bound for the parameter regime set in Fig. 4. Nor does the Helstrom bound provide accurate discrimination with an optimal single-shot measurement for the parameter regime set. A multishot Helstrom bound should be used instead, where N copies of a state are equivalent to N shots of the system. The multishot minimum probability of error between two states when there are N trials, only two states to discriminate and equal priors for either state [72] is

$$P_{\mathrm{err},N}^{\min} = \frac{1}{2}\left(1 - \left\|\frac{1}{2}(\hat{\rho}_1^{\otimes N} - \hat{\rho}_0^{\otimes N})\right\|\right), \tag{18}$$

where $||\hat{A}|| = \mathrm{Tr}(\sqrt{\hat{A}^{\dagger}\hat{A}})$ is the trace norm for a matrix $\hat{A}$. Focusing on the idler-click conditioned states only, the states upon the signal detector for when the object is present state $\hat{\rho}_1 = \hat{\rho}_{S|I,1}$ and absent $\hat{\rho}_0 = \hat{\rho}_{\mathrm{th}}(\bar{n}_{B,S})$. However, calculation of Eq. (18) is intractable due to the Hilbert-space dimensionality increasing dramatically with measurement trials N. Fortunately, the quantum Chernoff bound allows for easy calculation of the upper bound of

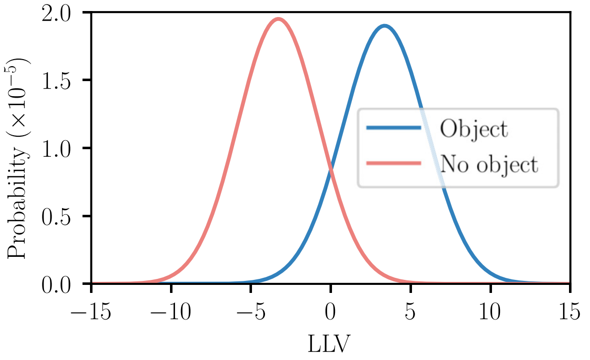

FIG. 5. Quantum illumination LLV probability distribution for both object present (colored blue) and absent (colored red) cases. $\bar{n} = 2.19 \times 10^{-2}$, $\eta_{S/I} = 0.5$, $\xi = 8.84 \times 10^{-3}$, $\bar{n}_{B,S} = 5.06 \times 10^{-2}$, $\bar{n}_{B,I} = 4.49 \times 10^{-4}$. The number of shots is 1.76×10^6 and the number of idler-click events displayed is 1.98×10^4.

the minimum error probability [2] via

$$P^{\min}_{\mathrm{err},N} \propto \frac{1}{2} e^{-N\zeta_{\mathrm{QCB}}}, \tag{19}$$

where $\zeta_{\mathrm{QCB}} = -\ln\left(\min_{0\leq s\leq 1} \mathrm{Tr}\left(\hat{\rho}_0^s \hat{\rho}_1^{1-s}\right)\right)$. We can compare this to the probability of error for the LLV framework when the detection decision threshold is set as LLV = 0,

$$P_{\mathrm{LLV:err}} = \frac{1}{2}\left(\int_{z=0}^{\infty} P_{\mathrm{H0}:\Lambda(x,\mu_I)}(z) + \right. \\ \left. + \int_{z=-\infty}^{0} P_{\mathrm{H1}:\Lambda(x,\mu_I)}(z)\right), \tag{20}$$

where z is a LLV, and $P_{\mathrm{H1/0}:\Lambda(x,\mu_I)}$ is the object present or absent LLV distribution when there has been mean idler clicks μ_I. Figure 6 shows the comparison of P_{err} for the LLV framework and the quantum Chernoff bound as a function of shots. We calculate the quantum Chernoff bound for QI (coincidence clicks only) using the number of trials $\lfloor \mathrm{Pr}_I \times N \rfloor$, this approach means we can fairly compare the quantum Chernoff bound for QI and CI, as CI has N trials. Here, we define $\lfloor x \rfloor$ as the floor function, which outputs the greatest integer less than or equal to x. A similar approach follows for setting the number of trials when discriminating between the idler no-click conditioned and object absent state. For the parameter regime in Fig. 6 there is only a negligible advantage to the inclusion of noncoincidence counts. This advantage is quantified by Eq. (25). In the multishot case, the LLV framework does not saturate the Helstrom bound. There is a simple reason for this. Click measurements at separate Geiger-mode detectors are not near optimal for the required task. They are, however, more resilient in difficult and realistic sensing environments.

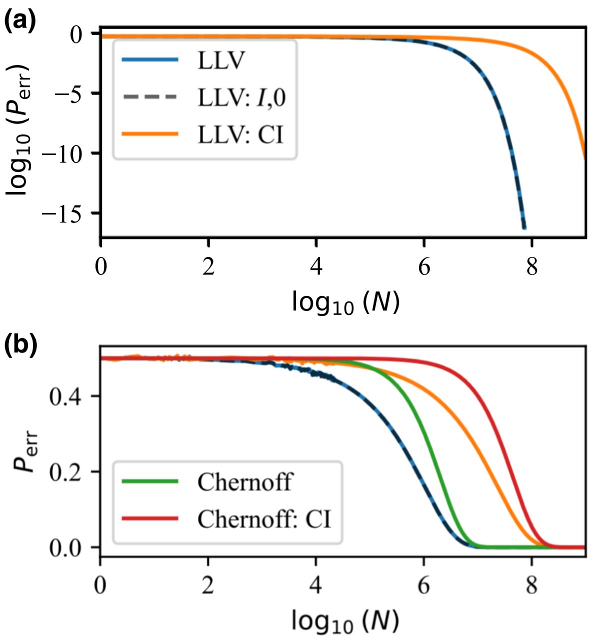

FIG. 6. Comparison of the quantum Chernoff bound and the probability of error of the LLV framework (for QI and CI). We also plot the probability of error of the QI LLV framework, which has the noncoincidence counts included too: LLV: I,0. Probability of error P_{err} on the y axis and shots N on the x axis. We have a log-log plot for (a) with P_{err} for LLV: QI, LLV: I,0 and LLV: CI plotted. For (b) the y axis is not a log plot but the x axis is. In (b) we plot P_{err} for LLV: QI, LLV: I,0, LLV: CI and Chernoff for QI and CI. The object present and absent states are being discriminated between. Mean photon number of the signal state $\bar{n} = 2.19 \times 10^{-2}$, system loss of all detectors $\eta_{S/I} = 0.5$, signal attenuation factor $\xi = 8.84 \times 10^{-3}$, mean photon number of background and dark counts for signal detector $\bar{n}_{B,S} = 5.06 \times 10^{-2}$, and mean photon number of background and dark counts for idler detector $\bar{n}_{B,I} = 4.49 \times 10^{-4}$. Monte Carlo simulation generated the earlier portion of this figure and analytic calculation in the Gaussian regime generated the remainder.

The lack of explicit calculation of an optimal performance bound for our multishot system can be solved by first acknowledging that our system belongs to a generalized class of sensing problems: quantum sensing in auxiliary-assisted phase-covariant optical channels [73]. The results in Ref. [73] have provided probe and measurement-independent ultimate performance bounds (expressed in the quantum Fisher information) for this class of sensing problems, subject to energy and mode-number constraints [74]. These performance bounds differ from the Helstrom bound discussed earlier as it makes no assumption about the probe state used. In particular, for phase-covariant Gaussian channels, N independent and identically distributed TMSV probes tends towards being the optimal probe as the mean photon number $\bar{n} \to 0$. For QI we do not discriminate using the TMSV, as we instead discriminate against the object absent state using the idler-click (no-click) conditioned states. These states are not the optimal probes. The optimality of CI is also discussed in Ref. [73]. Furthermore, while not optimal, our CI system can be enhanced by the use of threshold detection with photon-number-resolving detectors as explored in Ref. [75]. However, this enhancement is negligible for the parameter regimes we are concerned with weak signal strength $\bar{n} << 1$ and a low SNR $\bar{n} < \bar{n}_{\mathrm{B,S}}$.

B. Distinguishability measure

The distinguishability measure used here describes how much overlap there is between the object present and absent LLV distributions—effectively how much confidence can be ascribed to a decision of object present or absent given an LLV. Therefore, the distinguishability measure is a figure of merit (FOM), which characterizes system performance in confident detection decision making. The use of this FOM is in contrast with other FOMs, such as the SNR and the Cramér-Rao lower bound (CRLB) for signal loss estimation, which are not directly based on decision making. A qualitative comparison of FOMs is expanded upon in Appendix F. The Q function for a Gaussian distribution with LLV detection threshold d_{LLV}, mean μ, and standard deviation σ is

$$Q(d_{\mathrm{LLV}}, \mu, \sigma) = \frac{1}{\sqrt{2\pi}\sigma} \int_{d_{\mathrm{LLV}}}^{\infty} e^{-\left(\frac{z-\mu}{\sqrt{2}\sigma}\right)^2} dz. \tag{21}$$

We define the probability of detection and probability of false alarm, respectively, as

$$P_{\mathrm{D}}(d_{\mathrm{LLV}}) = Q(d_{\mathrm{LLV}}, \mu_{\mathrm{H1}:\Lambda(x,k)}, \sigma_{\mathrm{H1}:\Lambda(x,k)}) \tag{22}$$

and

$$P_{\mathrm{FA}}(d_{\mathrm{LLV}}) = Q(d_{\mathrm{LLV}}, \mu_{\mathrm{H0}:\Lambda(x,k)}, \sigma_{\mathrm{H0}:\Lambda(x,k)}). \tag{23}$$

The definitions in Eqs. (22) and (23) lead onto the distinguishability

$$\phi = 1 - [(1 - P_{\mathrm{D}}(0)) + P_{\mathrm{FA}}(0)]. \tag{24}$$

If we compare the distinguishability for a QI system that does $\phi_{I,0}$ and does not $\phi_{I,1}$ include noncoincidence clicks we can quantify the benefit of considering noncoincidence clicks. We quantify this benefit by defining a relative difference of distinguishabilities

$$\Delta\phi_{I,0} = \frac{\phi_{I,0} - \phi_{I,1}}{\phi_{I,1}} \times 100. \tag{25}$$

For the system parameters in Fig. 4, the noncoincidence relative advantage is $\Delta\phi_{I,0} = 0.3\%$. This is small, but there are regimes where the inclusion of noncoincidence clicks improves system performance significantly. For example, the benefit increases as the idler channel system loss parameter η_I decreases. The reduction of η_I means that the upsurge of signal clicks when an object is present is registered as a coincidence click less often, due to the low efficiency of registering idler clicks. To demonstrate that noncoincidence clicks are more useful in such regimes, we alter two parameters in Fig. 4. The new number of shots $N = 5 \times 10^7$ and idler loss parameter $\eta_I = 0.02$. With these values the noncoincidence relative advantage is $\Delta\phi_{I,0} = 24.47\%$, which is a significant benefit.

A threshold distinguishability ϕ_{t} is set to ensure that the effectiveness of the LLV test is consistent in different regimes. The threshold distinguishability uses the LLV distributions when there has been a mean number of idler clicks. An assumption is made that the underlying components of the distinguishability ϕ, P_{D}, and P_{FA}, are also consistent between regimes. Moreover, for a single regime each object present and absent LLV distribution distinguishability differs slightly according to the number of idler clicks k, hence the effectiveness of the LLV test differs with the number of idler clicks recorded. We ignore this discrepancy if it does not exceed the bound placed in Appendix G, and consider all likely LLV distributions for a regime to have a distinguishability set by the one calculated for the mean number of idler clicks. Clearly, the higher ϕ_{t} is, the more confident the detection decision. In this paper, threshold distinguishability is set to be $\phi_{\mathrm{t}} = 0.8$ in line with convention [46].

We define the number of shots required for threshold distinguishability

$$N_{\mathrm{t}} = \mathrm{int}\left(\frac{F^{-1}(\phi_{\mathrm{t}})}{\mathrm{Pr}_I}\right), \tag{26}$$

where $F^{-1}(\phi_{\mathrm{t}})$ is the inverse of the function ϕ_{t}, as derived in Appendix H. N_{t} allows for different parameter regimes to be compared fairly, as increasing the number of shots N increases ϕ, when $\phi < 1$.

While the system is running the return click rate can change. Hence, in order to analyze dynamically changing incoming data, a rolling window method is applied. We define the cumulative coincidence clicks after z time bins $T(z)$ and cumulative idler clicks $T_I(z)$, where z time bins is the number of shots that have been recorded. There is an initialization stage while $z < N_{\mathrm{t}}$. We have a LLV $R(z)$ for each time bin z defined as

$$R(z) = \Lambda(T(z) - T(z - N_{\mathrm{t}}), T_I(z) - T_I(z - N_{\mathrm{t}})), \tag{27}$$

for every time bin $z \geq N_{\mathrm{t}}$.

Figure 7 illustrates the change in LLV statistics between the object absent regime and the object present regime. The object suddenly appears at the time bin denoted by the vertical dashed line. The system fully updates from object absent to present regime over $z = N_{\mathrm{t}}$ time bins. Here, both regimes are separated by the threshold distinguishability ϕ_{t}.

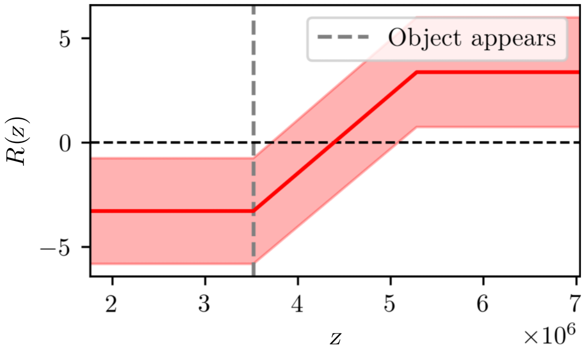

FIG. 7. Rolling window trajectory of QI mean LLV (solid line colored red) with a red shaded region limited by a standard deviation of error plus and minus the mean. Regime changes from object absent to present suddenly at time bin $z = 2N_{\rm t}$ marked by the vertical dashed line (colored gray). $N_{\rm t} = 1.76 \times 10^6$, $\bar{n} = 2.19 \times 10^{-2}$, $\eta_{S/I} = 0.5$, $\xi = 8.84 \times 10^{-3}$, $\bar{n}_{B,S} = 5.06 \times 10^{-2}$, $\bar{n}_{B,I} = 4.49 \times 10^{-4}$.

Hence Fig. 7 illustrates what $\phi_{\rm t}$ means for the distinctness of the object present and absent distributions. However, the duration of a shot is too short to process data practically in a rolling-window shot by shot. Instead a rolling window based on LLV samples every $N_{\rm t}$ shots is employed. This is elaborated upon in Sec. IV F with Eq. (35). The purpose of defining Eq. (27) is to visually show in Fig. 7 how our LLV framework can be applied to dynamic scenarios, whether it be shot by shot or LLV sample by sample for its refresh rate as shown in Eq. (35).

C. Comparing quantum illumination and classical illumination

System performance comparison of QI and CI using click counts directly is problematic as coincidence clicks and signal clicks are not the same, making it challenging to use click counts as a performance metric. Our framework addresses this problem by recasting click counts of any type into a LLV. For any system parameter regime, the object present and absent statistics for QI have a larger distinguishability than CI. We also define a quantum advantage QA as the ratio of the number of shots required for CI and QI to reach threshold distinguishability. Therefore, quantum advantage $\text{QA} = (N_{\rm t:CI}/N_{\rm t:QI})$, where $N_{\rm t:QI}$ is $N_{\rm t}$ shots required for threshold distinguishability for QI, and similarly for CI. In a physical system this quantity gives a reasonable approximation to the relative amount of time it would take for each system to determine the presence or otherwise of a target object under the same conditions. Figure 8 demonstrates that QI performs significantly better for all of the shown parameters. This advantage increases for low signal strength and high background-noise regimes.

On the other hand, a common-place approach for system performance is via a receiver operator curve (ROC). The ROC can be found by varying the LLV detection threshold $d_{\rm LLV}$ from $-\infty < d_{\rm LLV} < \infty$ and calculating $P_{\rm D}(d_{\rm LLV})$ and $P_{\rm FA}(d_{\rm LLV})$ accordingly.

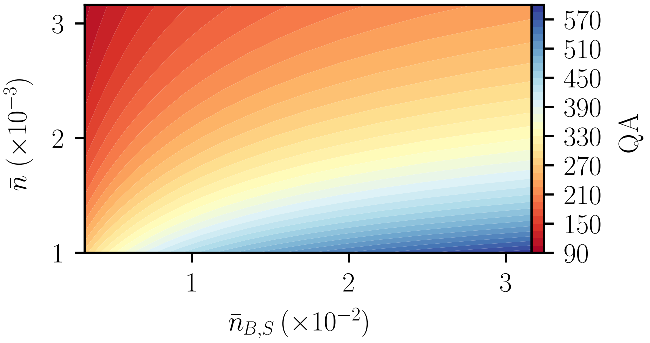

FIG. 8. Contour plot of quantum advantage $\text{QA} = (N_{\rm t:CI}/N_{\rm t:QI})$ for varied background noise and signal strength. $\eta_{S/I} = 0.5$, $\xi = 1.99 \times 10^{-2}$, and $\bar{n}_{B,I} = 4.49 \times 10^{-4}$.

Figure 9 compares two ROCs, one for CI and one for QI; clearly QI performs better than CI for the given parameters. To summarize, we have a method to assess system performance, which is self-calibrating, and if we relax the detection threshold $d_{\rm LLV}$ we have system performance in terms of a ROC.

IV. RANGE FINDING

A. Signal attenuation from distance

The process of interrogating a target object almost always results in attenuation of the signal strength. This attenuation is dependent on inclusion of realistic effects and object properties.

An object can be modeled as a Lambertian scatterer or a specular reflector. In this paper the Lambertian case is

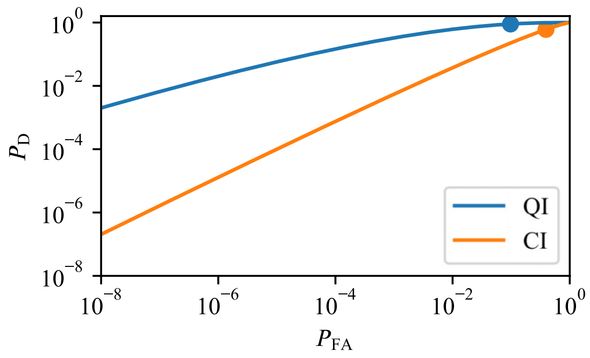

FIG. 9. Receiver operator curve for probability of detection $P_{\rm D}$ and probability of false alarm $P_{\rm FA}$ for QI and CI. The blue dot represents where the detection threshold for QI is set to $\text{LLV} = 0$ and the orange dots represent where the detection threshold for CI is set to $\text{LLV} = 0$. $\bar{n} = 2.19 \times 10^{-2}$, $\eta_{S/I} = 0.5$, $\xi = 8.84 \times 10^{-3}$, $\bar{n}_{B,S} = 5.06 \times 10^{-2}$, $\bar{n}_{B,I} = 4.49 \times 10^{-4}$, and $N = 1.76 \times 10^6$.

focused upon as the signal is scattered by the target into a large solid angle and the small solid angle subtended by the distant signal detector at the target provides a naturally dominant attenuation factor [76]. There are other possible attenuation effects such as beam divergence and any scattering or absorption from the medium between detector and object and these can be treated similarly. If instead we were to concentrate on a cooperative specular reflector beam divergence would be the dominant attenuation that is not intrinsic to the detectors.

The signal attenuation factor ξ, previously introduced in this paper, is now written in terms of interaction with a Lambertian scatterer. A model for signal attenuation using the averaged Lambert's cosine law, equal hemisphere of diffusion, and the inverse square law gives

$$\xi = \frac{\xi_{\mathrm{obj}} A_{\mathrm{d}}}{4\pi D^2}, \tag{28}$$

where ξ_{obj} is the intrinsic reflectivity of the object, with $\xi_{\mathrm{obj}} = 1$ as the case of a perfect reflector. The area of the detector is A_{d} and distance of object from the detector is D.

B. Expected click count and LLV as a function of distance

We would expect the number of shots to reach threshold N_{t} to increase with detector distance D. The change of signal attenuation with distance requires that a specific LLV after k idler clicks is defined for each distance D

$$\Lambda_D(\underline{x}, k) = \ln\left(\frac{P_{\mathrm{H1},D}(\underline{x}, k)}{P_{\mathrm{H0},D}(\underline{x}, k)}\right), \tag{29}$$

with $P_{\mathrm{H}\{1,0\},D}$ defined as the click-probability distribution for an object present and absent at distance D after N_{t} shots, respectively. Consequently, for any distance we can process data such that the effectiveness of the LLV test remains consistent. Assuming the requirement of processing $N_{\mathrm{t}}(D)$ shots for each distance D is satisfied, the expected mean coincidence click count $\mu_{\mathrm{D:I,1}}$ increases with distance due to the increased $N_{\mathrm{t}}(D)$. The mean LLV $\Lambda_D(\mu_{\mathrm{D:I,1}}, \mu_I)$ will stay approximately constant for all inspected distances, as the LLV test effectiveness is consistent. Hence, the different distances can have their data streams directly compared, which is a valuable feature for a range-finding protocol.

C. Delay and distance

Light takes time to travel, therefore there will be a temporal mismatch between the idler and signal beams returning to the detectors due to the different path lengths traveled. In order to retrieve the light source's temporal correlations this mismatch must be accounted for, in the form of the expected delay. The incoming binary stream of click events at the detector is henceforth referred to as the idler or signal stream. The idler stream is set to have zero delay, as it is locally measured with a known path length. For simplicity the system we assume is monostatic. Therefore, the detectors and light source are located approximately at the same location, which simplifies the relation for the expected delay. The extension to bistatic is straightforward. The expected time delay for the signal beam when an object is at distance D from the detector is therefore

$$t(D) = \frac{2D}{c}, \tag{30}$$

where c is the speed of light.

D. Discretizing the delay

As the model considers the idler and signal beam data streams to be in discrete time bins the expected delay must be discretized in order to match the signal stream with idler. The expected delay in shots for an object at distance D from the detector is

$$M_{\mathrm{delay}}(D) = \lfloor \big(t(D) f_{\mathrm{rep}}\big) \rfloor. \tag{31}$$

Therefore, the idler stream is matched with the signal stream shifted back $M_{\mathrm{delay}}(D)$ shots, for an inspected distance of D. The optimal spatial resolution of the system is set by the source repetition rate f_{rep}

$$D_p = \frac{c}{2 f_{\mathrm{rep}}}. \tag{32}$$

Some error can occur due to the discretized delay not properly matching with object distances that are not integer values of the spatial resolution. This protocol's range-finding abilities will also be tempered by the misbinning stemming from timing jitter, but this effect is neglected here, as mentioned earlier. Previous literature for simple detection-based QI range finding describes timing jitter corresponding to approximately equal to 10 cm range uncertainty [77], which is smaller than the range resolution we specify. The temporal analogue of the optimal spatial resolution is the optimal temporal resolution $t_{\mathrm{optimal}}(D)$, which determines how quickly our system can make a confident measurement for a distance D. This depends on the source repetition rate f_{rep} and the threshold distinguishability ϕ_{t} as defined in

$$t_{\mathrm{optimal}}(D) = \frac{N_{\mathrm{t}}(D)}{f_{\mathrm{rep}}}. \tag{33}$$

E. LLV range-finding statistics

In a range-finding scenario the distance of a possible target object is unknown, and hence the expected delay is also

TABLE I. Shots required N_{t} for threshold distinguishability $\phi_{\mathrm{t}} = 0.8$ and return signal delay in shots for target object distance D from detector $M_{\mathrm{delay}}(D)$. Lambertian scatterer. Source pulse repetition rate $f_{\mathrm{rep}} = 0.5$ GHz. $\bar{n} = 2.19 \times 10^{-2}$, $\eta_{S/I} = 0.5$, $\xi_{\mathrm{obj}} = 1$, $\bar{n}_{B,S} = 5.06 \times 10^{-2}$, $\bar{n}_{B,I} = 4.49 \times 10^{-4}$.

Distance (m)	N_{t}	$M_{\mathrm{delay}}(D)$	ξ
1.2	5.29×10^{4}	4	5.53×10^{-2}
3	1.76×10^{6}	10	8.84×10^{-3}
3.3	2.56×10^{6}	11	7.31×10^{-3}
6	2.73×10^{7}	20	2.21×10^{-3}
CI: 3	3.91×10^{7}	10	8.84×10^{-3}

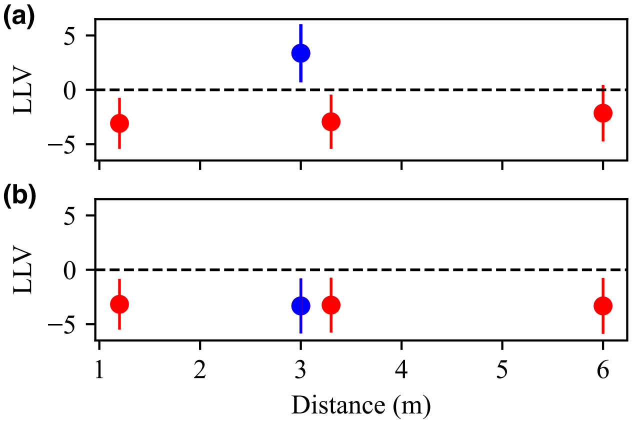

FIG. 10. LLV of simulated range-finding statistics (a) when an object is situated at a distance 3 m and (b) when an object is absent. Mean and one standard deviation error bar plus and minus the mean plotted. The correct distance 3 m is shown as a blue dot and error bar. The shots required for threshold distinguishability N_{t}, signal stream delay in shots $M_{\mathrm{delay}}(D)$ for each object distance, and ξ is given in Table I. The horizontal (black) dashed line is when the LLV $= 0$ $\bar{n} = 2.19 \times 10^{-2}$, $\eta_{S/I} = 0.5$, signal attenuation is modelled by the reflection of a perfect Lambertian scatterer at distance D, $\bar{n}_{B,S} = 5.06 \times 10^{-2}$, and $\bar{n}_{B,I} = 4.49 \times 10^{-4}$. Results of 10^{4} simulations.

unknown. We systematically work through different possible distances from near to far. Other than the set of model parameters, which determine the expected object statistics, there are two pieces of information that the operator can control when searching for an object: how long does it take to acquire confident statistics N_{t} and what delay should be used to match streams correctly $M_{\mathrm{delay}}(D)$. Table I shows N_{t} and $M_{\mathrm{delay}}(D)$ for a set of inspected distances.

In the parameter regime set, for all inspected distances, the expected object present mean LLV is $\mu_{\mathrm{E}} \approx 3.36$, knowledge of this value helps consideration towards which searched distance is correct. Simulated incoming data is processed into the LLV for that inspected distance $\Lambda_D(x, k)$ with the corresponding delay $M_{\mathrm{delay}}(D)$. Figure 10 displays the mean LLV for each inspected distance distribution μ_{G}, for both cases of an object absent and a stationary object set to be at a distance of 3 m. An error bar of one standard deviation is also plotted. These statistics have been generated from many Monte Carlo simulation runs and each simulation run uses the same seed click data to process all inspected distances. Although it is worthwhile to note that this is not what would be seen in a real-time range-finding protocol, as the statistics for the far distance take longer to acquire than the near distance, therefore some near-distance statistics have been discarded in order to match the quantity of simulation results. In Fig. 10 for the object present case, the correctly inspected distance 3 m shows a strong signature, due to the correct coincidence matching. However, all of the falsely inspected distances display varying levels of a shifted LLV from H0, this is due to the mismatch caused by the incoming data not adhering to the H1 or H0 statistics for that inspected distance. Whereas, for an object absent, all inspected distance statistics match their respective object absent statistical outcome.

The results from Fig. 10 can be interpreted as follows. The closer $\mu_{\mathrm{G}} - \mu_{\mathrm{E}} \to 0$, the closer that particular inspected distance infers that an object is actually situated at that distance. This interpretation comes with the caveat that a nearer and correct distance has not been overlooked, as a sufficiently far searched distance can also tend $\mu_{\mathrm{G}} - \mu_{\mathrm{E}} \to 0$ due to the LLV shift. The searched distances are relatively near for LIDAR standards, this is because we are using an uncooperative Lambertian target in the simulation, a cooperative specular target would allow for ranging to perform well at considerably longer distances.

F. Simulated example of a range-finding detection scenario

Now that the LLV dynamics for different inspected distances have been shown, a real-time range-finding protocol is described. In order to compare LLV measurements fairly from different inspected distances we must ensure that each measurement is formed from its corresponding shots required for threshold distinguishability $N_{\mathrm{t}}(D)$. Hence, for each inspected distance D a LLV sample is taken every $N_{\mathrm{t}}(D)$ shots. We define a set of K LLV measurements as $\{\Lambda_1, \ldots, \Lambda_K\}$, with each sample separated temporally by $N_{\mathrm{t}}(D)$ shots. After accumulating a number S of LLV samples it is possible to calculate the sample mean, $\mu_S = ((\Sigma_{i=1}^{S} \Lambda_i)/S)$.

Plotted in Fig. 11 is the mean LLV $\mu_S(D)$ of a simulated signal for an accumulated number of S LLV samples every $N_{\mathrm{t}}(D)$ shots. The number of samples that comprise $\mu_S(D)$ increases with the elapsed time M_{elapsed} in shots. In Fig. 11 the trajectory for each inspected distance D has a different length as each one has a different total number of samples within the elapsed time. Each sample needs $N_{\mathrm{t}}(D)$ shots so until this number of shots is reached the trajectory does

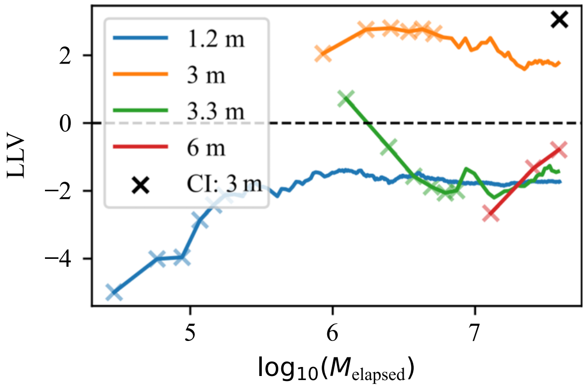

FIG. 11. Real-time signal trajectory of μ_S for the near (1.2 m), correct (3 m), one delay bin after correct (3.3 m), and far (6 m) inspected distances. With μ_S on the y axis and elapsed time in shots M_{elapsed} on the x axis. The horizontal (black) dashed line is when the LLV $= 0$. The total elapsed time in shots is N_{t}(CI:3 m). The object situated at a distance 3 m. N_{t}, $M_{\mathrm{delay}}(D)$, and ξ given in Table I. $f_{\mathrm{rep}} = 0.5$ GHz, $\bar{n} = 2.19 \times 10^{-2}$, $\eta_{S/I} = 0.5$, signal attenuation is modeled by the reflection off a perfect Lambertian scatterer at distance D, $\bar{n}_{B,S} = 5.06 \times 10^{-2}$, and $\bar{n}_{B,I} = 4.49 \times 10^{-4}$.

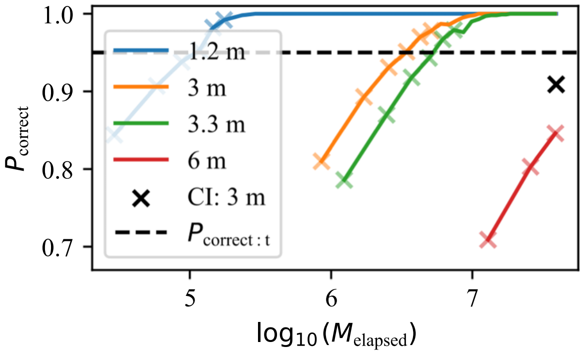

FIG. 12. Real-time trajectory of P_{correct} for the near (1.2 m), correct (3 m), one delay bin after correct 3.3 m, and far (6 m) inspected distance. With P_{correct} on the y axis and elapsed time M_{elapsed} on the x axis. The total elapsed time in shots is N_{t}(CI:3 m). The object situated at a distance 3 m. N_{t}, $M_{\mathrm{delay}}(D)$, and ξ given in Table I. $f_{\mathrm{rep}} = 0.5$ GHz, $\bar{n} = 2.19 \times 10^{-2}$, $\eta_{S/I} = 0.5$, signal attenuation is modeled by the reflection off a perfect Lambertian scatterer at distance D, $\bar{n}_{B,S} = 5.06 \times 10^{-2}$, and $\bar{n}_{B,I} = 4.492 \times 10^{-4}$. This figure displays the statistics of 10^3 different simulation runs, in order to generate the P_{correct} distribution.

not start. In Fig. 11 each inspected distance trajectory has its first six samples plotted as a cross. Furthermore, for the sake of clarity we omit plotting a cross for sample numbers greater than six. A 3-m inspected distance stream for CI is also plotted, QI's advantage is clear as the first LLV sample occurs well before CI's first sample, this means that detection decisions can be made sooner for QI than CI, which corresponds to a more responsive object-detection system. A false decision is made for the near inspected distance (1.2 m) around $M_{\mathrm{elapsed}} \approx 5 \times 10^4$ shots; however, it can also be seen that this inspected distance later converges to the correct decision with $\mu_{\mathrm{G}}(1.2\ \mathrm{m}) = -3.08$ relatively quickly. Consequently, confident detection decisions are made sooner for distances searched nearest to the detector, as there is a larger number of samples for convergence to occur. The search for an object is executed by scanning from near to far. The range-finding protocol stops scanning outwards once there is a signature of an object at a distance D. Useful to note, is that samples can be made sooner for any inspected distance, at the expense of detection decision error and comparability of LLV between inspected distances. Recording a sample sooner would mean that the shots $N < N_{\mathrm{t}}(D)$, this would cause P_{D} to decrease and P_{FA} to increase due to the larger overlap with a smaller integration time.

An object-detection decision is made when the nearest inspected distance any $\mu_s > 0$. Conversely, if $\mu_s \leq 0$ a decision is made that an object is not present at that distance. Many simulation runs of an incoming signal are performed to generate a distribution of detection decisions along elapsed time M_{elapsed} in shots. For the inspected distances, excluding the furthermost, as time progresses the probability of a correct decision P_{correct} improves. This is displayed in Fig. 12. Moreover, Fig. 12 shows the number of samples required S for P_{correct} to reach an acceptable threshold $P_{\mathrm{correct:t}} = 0.95$. In Fig. 12, similar to Fig. 11, each inspected distance trajectory has its first six samples plotted as a cross. As follows, the realistic temporal resolution for a distance D when the target object is at a distance D_{correct} is

$$t_{\mathrm{realistic}}(D; D_{\mathrm{correct}}) = S \times t_{\mathrm{optimal}}(D). \tag{34}$$

This trend of an improvement of P_{correct} with time fails for inspected distances too far from the correct location. As the mean of a sufficiently far searched distance D $\mu_{\mathrm{G}}(D) \geq 0$. However, this situation is avoided as the correct inspected distance is decided upon before enough far away searches reach its realistic temporal resolution.

Monitoring a set of inspected distances of mean LLVs for an accumulated sample number of S samples μ_S, with a rolling window refresh rate of S allows the operator to exclude the presence of an object at near distances while searching outwards to hone in on its true location. The rolling window allows for dynamic monitoring of the range of the object. Hence, the sample rolling window is defined as

$$R(\tilde{s}) = \frac{1}{S} \sum_{i=\tilde{s}-S+1}^{\tilde{s}} \Lambda_i, \tag{35}$$

for any sample number $\tilde{s}$ such that $S \leq \tilde{s} \leq K$. This moving average rolling window defined in Eq. (35) is what is practically used when analyzing real data, as signal processing with the rolling window defined by shots in Eq. (27) is unfeasible due to the very short temporal duration of a shot. An incoming signal is more easily processed with the sample rolling window applied. This leads to the definition of the average distinguishability, which is the distinguishability of object present and absent LLV distributions with a moving average of S samples applied,

$$\phi_{\text{average}}(S) = 1 - \left(- \Phi\left(0, \mu_{\text{H1}:\Lambda(x,\mu_I)}, \frac{\sigma_{\text{H1}:\Lambda(x,\mu_I)}}{\sqrt{S}}\right) + \right. \\ \left. + \Phi\left(0, \mu_{\text{H0}:\Lambda(x,\mu_I)}, \frac{\sigma_{\text{H0}:\Lambda(x,\mu_I)}}{\sqrt{S}}\right)\right). \quad (36)$$

Clearly when $S = 1$ this equation reduces to the distinguishability defined in Eq. (24) after mean idler clicks.

V. DISCUSSION

In this paper a theory for target object detection and range finding using pulsed two-mode quantum states with Geiger-mode click detectors has been provided. We have provided a physical justification for the use of our model, based on the fact that after interaction with the object the two states at the signal detector are only marginally different. Not only this, but the measurements that we envisage, although practical, are far from optimal for the discrimination of a target. This makes the use of a simple, powerful statistical tool necessary to detect objects for reasonable values of noise and loss parameters. Our model uses the log-likelihood value to do this. It also facilitates comparison of quantum and classical illumination (with thermal statistics) to demonstrate which values of system parameters ensure a quantum advantage in a particular object-detection scenario.

Our model of the source state of light and detectors is written in the Fock basis formalism, because detector click probabilities are naturally expressed in this basis. These probabilities are based on different heralded signal states being produced by idler detector measurements. After many shots, from these click probabilities, click-count probability distributions are generated. The distributions can be used to form a log-likelihood value, which provides information about the relative sizes of the probabilities that the target is present and absent. This turns out to be a more useful measure for inference of a target object's presence than the click-count data by itself. Each click count has a corresponding log-likelihood value, therefore the click-count distributions are transformed into log-likelihood value distributions. Ease of, and confidence in, detecting an object is determined by the distinguishability of the object present and absent log-likelihood distributions. This log-likelihood value framework can allow for multichannel detector click data to be transformed into a single value. Therefore, this approach includes noncoincidence clicks, which are often overlooked by other quantum illumination object detection protocols. Inference using this metric also facilitates different inspected distances of the system parameters to be compared fairly for effectiveness of the log-likelihood value test, comparison of different inspected distances is required for the range-finding aspect of the protocol. Consideration for fair comparison is particularly desired for a Lambertian reflecting target, as system parameters differ for each inspected distance. Moreover, this theory is also frequency independent, allowing for extension beyond LIDAR in the optical frequency regime.

Simulation results using the protocol reinforce the knowledge that quantum illumination with click detectors performs better than classical illumination in low signal strength and high background-noise regimes. This quantum advantage persists even in lossy and noisy situations with simple click detectors capable of operating in free space. The origin of the quantum advantage is in the photon-number correlations between the two spatially separated beams of the source state. Hence, any click measurement at the idler detector conditions the probability of a click event at the signal detector to increase. In this QI-based protocol the driving force of the quantum advantage is the incidence of coincidence clicks. These occur when both the idler and the signal detectors record a click. The idler and signal detector provides a binary data stream each of a click or a no-click event. Photons from our light source will have a delay in the signal stream compared to the idler stream, whereby this delay is according to a possible target object distance. A chosen delay is set and coincidence (and noncoincidence) click counts are accumulated from these detector data streams, to which they are processed into log-likelihood values. Searching through different delays and processing detector data into log-likelihood values is how we perform range finding of a target object. The correctly inspected distance, and hence delay, will return statistics that are distinguishable from the false inspected distances. This is due to the reflected light from the object that causes a signal click being properly matched with its counterpart idler click, thus recovering the nonclassical photon-number correlations between the two beams.

This experimentally motivated theoretical framework has recently been applied to demonstrate the functionality of a quantum-enhanced LIDAR protocol for performing range finding robust to classical jamming [55]. Further work will involve extension to multimode quantum illumination, such as modes based on spectral information. This will improve quantum illumination's performance. Work will also be undertaken to recognize and remove jamming attempts, which will improve the versatility of this protocol in dynamic and perhaps hostile situations.

ACKNOWLEDGMENTS

The authors thank Mateusz P. Mrozowski for useful discussions. This work is funded by the UK Ministry of Defence. The data presented in this work are available at Ref. [78]. J.J. would like to thank the UK Engineering and Physical Sciences Research Council for funding via the UK National Quantum Technology Programme and the QuantIC Imaging Hub (Grant No. EP/T00097X/1).

APPENDIX A: POVM DERIVATION

Deriving the generic no-click POVM element for a given mode. The parameter ζ is used to represent a generic factor, which accounts for all factors of loss of the signal state. Additionally, a generic background-noise mean photon number $\bar{n}_B$ is used here. Here, the mode labeling is mode 0 for the background-noise port, mode 1 for the light-source state port, mode 2 for the neglected port, and mode 3 for the click-detector port. The probability of a no-click event is given by

$$\mathrm{Pr}_x = \mathrm{Tr}\left(\mathrm{Tr}_2(\hat{U}\hat{\rho}_{\mathrm{th}} \otimes \hat{\rho}\hat{U}^\dagger)|0\rangle_3\langle 0|\right), \tag{A1}$$

where the beam-splitter operator is defined as

$$\hat{U} = e^{-i\arccos(\sqrt{\zeta})(\hat{a}_0^\dagger \hat{a}_1 + \hat{a}_0 \hat{a}_1^\dagger)}. \tag{A2}$$

The probability of no click can also be defined by using a POVM element

$$\mathrm{Pr}_x = \mathrm{Tr}\left(\hat{\rho}\hat{\pi}_{\times,3}\right). \tag{A3}$$

Rearranging Eq. (A1) to find the no-click POVM element for mode 3

$$\hat{\pi}_{\times,3} = \mathrm{Tr}_0\left((\hat{\rho}_{\mathrm{th}} \otimes \hat{1})\hat{U}^\dagger(\hat{1} \otimes |0\rangle\langle 0|)\hat{U}\right). \tag{A4}$$

The following derivation finds a closed-form summation over the Fock basis for Eq. (A4). The use of the coherent state basis throughout this derivation will be of great use. Firstly,

$$\begin{aligned}\hat{U}^\dagger(\hat{1} \otimes |0\rangle\langle 0|)\hat{U} &= \frac{1}{\pi}\hat{U}^\dagger \int d^2\alpha |\alpha\rangle_2\langle\alpha| \otimes |0\rangle_3\langle 0|\hat{U}.\\ &= \frac{1}{\pi}\int d^2\alpha |t^*\alpha\rangle_0\langle t^*\alpha| \otimes |r^*\alpha\rangle_1\langle r^*\alpha|,\end{aligned} \tag{A5}$$

and

$$\hat{\rho}_{\mathrm{th}} \otimes \hat{1} = \frac{1}{\pi\bar{n}_B}\int d^2\beta |\beta\rangle_0\langle\beta| \otimes \hat{1}_1. \tag{A6}$$

Hence, with substitution of Eqs. (A5) and (A6) into Eq. (A4) yields

$$\begin{aligned}\hat{\pi}_{\times,3} &= \frac{1}{\pi^3\bar{n}_B}\int d^2\beta d^2\alpha d^2\gamma e^{\frac{-|\beta|^2}{\bar{n}_B}}\\ &\quad \times \langle\gamma|\beta\rangle\langle\beta|t^*\alpha\rangle\langle t^*\alpha|\gamma\rangle \otimes |r^*\alpha\rangle_3\langle r^*\alpha|, \qquad \text{(A7)}\\ &= \frac{1}{\pi^2\bar{n}_B|r|^2}\int e^{-|\beta|^2\frac{\bar{n}_B+1}{\bar{n}_B} - \frac{|t|^2}{|r|^2}|\tilde{\alpha}|^2 + \beta^*\frac{t^*}{r^*}\tilde{\alpha}}\\ &\quad \times e^{\beta\frac{t}{r}\tilde{\alpha}^*} d^2\tilde{\alpha} d^2\beta |\tilde{\alpha}\rangle_3\langle\tilde{\alpha}|. \qquad \text{(A8)}\end{aligned}$$

In the above derivation a change of variable is employed $\tilde{\alpha} = r^*\alpha$, hence $d^2\alpha = (d^2\tilde{\alpha}/|r|^2)$, and thus $\gamma = \gamma_r + i\gamma_i$ is decomposed into real and imaginary parts to compute this integral as $d^2\gamma = d\mathcal{R}(\gamma)d\mathcal{I}(\gamma)$, which allows each component to be expressed as a well-known Gaussian integral for an analytic solution. Similarly, the $d^2\beta$ integral is solved by this real and complex decomposition.

$$\hat{\pi}_{\times,3} = \frac{1}{\pi|r|^2(\bar{n}_B + 1)}\int d^2\tilde{\alpha} e^{-|\tilde{\alpha}|^2\frac{|t|^2}{|r|^2}\frac{1}{\bar{n}_B+1}}|\tilde{\alpha}\rangle_3\langle\tilde{\alpha}|. \tag{A9}$$

Setting $\bar{b} = (|r|^2/|t|^2)(\bar{n}_B + 1)$ displays Eq. (A9) in the P representation of a single-mode thermal state with mean photon number $\bar{b}$ with a factor of $|t|^{-2}$ in front [79]

$$\hat{\pi}_{\times,3} = \frac{1}{\pi|t|^2\bar{b}}\int d^2\tilde{\alpha} e^{\frac{-|\tilde{\alpha}|^2}{\bar{b}}}|\tilde{\alpha}\rangle\langle\tilde{\alpha}|. \tag{A10}$$

As the measured background-noise thermal-state mean photon number $\bar{n}_B^{'}$ is to be unaffected by the reflection parameter of the beam splitter the scaled background-noise thermal-state mean photon number is thus defined as $\bar{n}_B = ((\bar{n}_B^{'})/|r|^2)$. The transmission and reflection parameters of the beam splitter adhere to $|t|^2 + |r|^2 = 1$, therefore the transmission magnitude $|t|^2 = \zeta$ and reflection magnitude $|r|^2 = 1 - \zeta$. Converting Eq. (A10) into the Fock basis and substituting in the mean photon number scaling, the generic no-click POVM element with measured background noise $\bar{n}_B^{'}$ unaffected by the POVM element for mode A is

$$\hat{\pi}_{\times,A}(\zeta, \bar{n}_B^{\prime}) = \frac{1}{\bar{n}_B^{\prime} + 1}\sum_{n=0}^{\infty}\left(\frac{\bar{n}_B^{\prime} + 1 - \zeta}{\bar{n}_B^{\prime} + 1}\right)^n |n\rangle_A\langle n|. \tag{A11}$$

Consequently, the generic click POVM element for mode A is

$$\hat{\pi}_{\checkmark,A}(\zeta, \bar{n}_B^{\prime}) = \hat{1}_A - \hat{\pi}_{\times,A}(\zeta, \bar{n}_B^{\prime}). \tag{A12}$$

APPENDIX B: PHOTON-NUMBER DISTRIBUTION DERIVATION

The photon-number distributions of the states incident upon the signal detector, when in the presence of noise, system loss, and signal attenuation are derived in this Appendix. Use of the coherent-state basis in these derivations is wise, due to the beam splitters required to model the mixing of states of light and the inclusion of parameters such as system loss and signal attenuation. The density matrix of the unconditioned state is

$$\hat{\rho}_S = \mathrm{Tr}_3\left(\hat{U}\mathrm{Tr}_I(\hat{\rho}_{\mathrm{TMSV}}) \otimes \hat{\rho}_{B,S}\left(\frac{\bar{n}_{B,S}}{1-\xi\eta}\right)\hat{U}^{\dagger}\right), \tag{B1}$$

$$= \hat{\rho}_{\mathrm{th}}(\xi\eta_S\bar{n} + \bar{n}_{B,S}), \tag{B2}$$

where mode 3 is the neglected output of the beam splitter, and the beam splitter has a transmission parameter $|t|^2 = \xi\eta_S$. Therefore, the unconditioned-state photon-number distribution is

$$P(n)_S = \frac{(\xi\eta_S\bar{n} + \bar{n}_{B,S})^n}{(\xi\eta_S\bar{n} + \bar{n}_{B,S} + 1)^{(n+1)}}. \tag{B3}$$

The density matrix of the idler no click conditioned state before it is incident on the signal detector is

$$\hat{\rho}_{\mathrm{I|X}} = \frac{\mathrm{Tr}_I(\hat{\rho}_{\mathrm{TMSV}}(\hat{1} - \hat{\pi}_I))}{1 - \mathrm{Pr}_I}, \tag{B4}$$

$$= \hat{\rho}_{\mathrm{th}}(\bar{n}_{\mathrm{X}}), \tag{B5}$$

where $\bar{n}_{\mathrm{X}} = \bar{n}((1 + \bar{n}_{B,I} - \eta_I)/(1 + \bar{n}_{B,I} + \bar{n}\eta_I))$. Following a similar process as earlier with beam splitters in Eq. (B1), the idler no-click conditioned state is

$$\hat{\rho}_{S|I,0} = \hat{\rho}_{\mathrm{th}}(\xi\eta_S\bar{n}_{\mathrm{X}} + \bar{n}_{B,S}), \tag{B6}$$

with its photon-number distribution as

$$P(n)_{S|I,0} = \frac{(\xi\eta_S\bar{n}_{\mathrm{X}} + \bar{n}_{B,S})^n}{(\xi\eta_S\bar{n}_{\mathrm{X}} + \bar{n}_{B,S} + 1)^{(n+1)}}. \tag{B7}$$

Ease of calculation afforded by considering the idler-click conditioned state as a thermal-difference state [80]. The idler-click conditioned-state density matrix before it is incident on the signal detector is

$$\hat{\rho}_{\mathrm{I}|\checkmark} = \frac{1}{\mathrm{Pr}_I}\left(\hat{\rho}_{\mathrm{th}}(\bar{n}) - (1 - \mathrm{Pr}_I)\hat{\rho}_{\mathrm{th}}(\bar{n}_{\mathrm{X}})\right). \tag{B8}$$

The idler-click conditioned-state density matrix is therefore

$$\hat{\rho}_{S|I,1} = \frac{1}{\mathrm{Pr}_I}\Bigg(\hat{\rho}_{\mathrm{th}}(\xi\eta_S\bar{n} + \bar{n}_{B,S}) - \\ - (1 - \mathrm{Pr}_I)\hat{\rho}_{\mathrm{th}}(\xi\eta_S\bar{n}_{\mathrm{X}} + \bar{n}_{B,S})\Bigg), \tag{B9}$$

hence its photon-number distribution is

$$P(n)_{I,1} = \frac{1}{\mathrm{Pr}_I}\Bigg(\frac{(\xi\eta_S\bar{n} + \bar{n}_{B,S})^n}{(\xi\eta_S\bar{n} + \bar{n}_{B,S} + 1)^{(n+1)}} - \\ - (1 - \mathrm{Pr}_I)\frac{(\xi\eta_S\bar{n}_{\mathrm{X}} + \bar{n}_{B,S})^n}{(\xi\eta_S\bar{n}_{\mathrm{X}} + \bar{n}_{B,S} + 1)^{(n+1)}}\Bigg). \tag{B10}$$

Closed-form representations of the coincident (and noncoincident) click probabilities can also be found from the complement of $P(n)_{I,1}$ [and $P(n)_{I,0}$] by setting $n = 0$.

APPENDIX C: GAUSSIAN APPROXIMATION

Analytic simplicity and computational speed is afforded by operating in the Gaussian regime. This regime is the system parameters such that the binomial click-count distributions can be approximated as Gaussian distributions, with negligible error produced. The following criteria is applied to ensure the Gaussian approximation is valid for the system parameter set. The criteria is that all binomial distributions for the system parameters in question must not be too skewed. In other words, this inequality must be satisfied

$$\frac{1 - 2p}{\sqrt{Np(1-p)}} < 0.3. \tag{C1}$$

Here p is the probability that underlies the binomial distribution and N is the number of shots. In practice not all binomial distributions need to be checked, instead only the binomial distribution that is most prone to failing the criteria to be in the Gaussian regime are checked. In the case of low signal strength in a noisy and lossy environment, the weakest distribution is the object absent signal coincidence click-count distribution after a thresholded minimum of idler clicks. The mean and standard deviation of the idler-click distribution is μ_I and σ_I, respectively. These statistical moments for the idler distribution are derived from the probability of an idler click Pr_I and number of shots N. The thresholded minimum of idler clicks is $I_{\mathrm{min}} = \lfloor(\mu_I - 4\sigma_I)\rfloor$. Hence the weakest distribution has the form

$$P_{\mathrm{min}}(x) = \binom{I_{\mathrm{min}}}{x} p_{\mathrm{min}}^x (1 - p_{\mathrm{min}})^{I_{\mathrm{min}} - x}, \tag{C2}$$

where p_{min} is the least likely type of signal click event in the analyzed system when the object is absent. The least likely type of signal click event for the system is the coincidence click. If this distribution satisfies Eq. (C1) then the Gaussian approximation is valid for the given system parameters. Once it has been demonstrated that the Gaussian regime can be operated in, any binomial distribution pertaining to those system parameters is transformed from

$$P(x,N,p) = \binom{N}{x} p^{x}(1-p)^{N-x}. \tag{C3}$$

to

$$P(x,N,p) \approx \frac{1}{\sigma\sqrt{2\pi}} e^{-0.5\left(\frac{x-\mu}{\sigma}\right)^{2}}, \tag{C4}$$

where $\mu = Np$ and $\sigma = \sqrt{Np(1-p)}$.

APPENDIX D: DERIVING THE LINEAR FORM OF THE LLV

The generic LLV in its ratio of click-probability distributions form

$$\Lambda(\underline{x},k) = \ln\left(\frac{P_{\mathrm{H1}}(\underline{x},k)}{P_{\mathrm{H0}}(\underline{x},k)}\right), \tag{D1}$$

$\underline{x}$ is the vector of the click counts by type of click event, k is the relevant number of shots (CI total shots and QI number of idler clicks), and $P_{\mathrm{H}\{1,0\}}(\underline{x},k)$ is the probability for object present or absent, respectively. The probability distribution for click events is originally binomial, due to the Bernoulli trials undertaken. For the remainder of the Appendices, we use shorthand notation for the click probabilities $\mathrm{Pr}_{\mathrm{H1:CI}} \equiv p_{\mathrm{H1}}$, $\mathrm{Pr}_{\mathrm{H0:CI}} \equiv p_{\mathrm{H0}}$, $\mathrm{Pr}_{I} \equiv p_{I}$, $\mathrm{Pr}_{S|I,1} \equiv p_{S|I,1}$, $\mathrm{Pr}_{S|I,0} \equiv p_{S|I,0}$, and $\mathrm{Pr}_{\mathrm{H0}} \equiv p_{\mathrm{H0}}$. The simpler CI case is focused on first, as there is only one element in $\underline{x} \equiv x$. The object present and absent probability density functions in its binomial form, respectively,

$$P_{\mathrm{H1}}(x,N) = \binom{N}{x} p_{\mathrm{H1}}^{x}(1-p_{\mathrm{H1}})^{N-x}, \tag{D2}$$

$$P_{\mathrm{H0}}(x,N) = \binom{N}{x} p_{\mathrm{H0}}^{x}(1-p_{\mathrm{H0}})^{N-x}. \tag{D3}$$

As N, x, and all the click probabilities are all real and positive Eq. (D1) can be expressed as a linear equation. Hence, for CI, Eq. (D1) is

$$\Lambda(x,N) = Mx + NC, \tag{D4}$$

where $M = \ln\left(\frac{p_{\mathrm{H1}}(1-p_{\mathrm{H0}})}{p_{\mathrm{H0}}(1-p_{\mathrm{H1}})}\right)$ and $C = \ln((1-p_{\mathrm{H1}}/1-p_{\mathrm{H0}}))$. The LLV transformation for QI easily extends to include idler not firing events in the linear equation. The signal click count x after k idler-click events and signal click count y after $N-k$ idler no-firing events in the QI protocol is transformed by the LLV defined as

$$\Lambda(\underline{x},k) = \underline{M}^{\mathrm{T}}\underline{x} + \underline{N}\underline{C}^{\mathrm{T}}, \tag{D5}$$

where $\underline{M}^{\mathrm{T}} = (M_1\ M_2)$, $\underline{x} = (x\ y)$, $\underline{C}^{\mathrm{T}} = (C_1\ C_2)$, and $\underline{N} = \binom{k}{N-k}$. Here

$$M_1 = \ln\left(\frac{p_{S|I,1}(1-p_{\mathrm{H0}})}{p_{\mathrm{H0}}(1-p_{S|I,1})}\right), \tag{D6}$$

$$M_2 = \ln\left(\frac{p_{S|I,0}(1-p_{\mathrm{H0}})}{p_{\mathrm{H0}}(1-p_{S|I,0})}\right), \tag{D7}$$

$$C_1 = \ln\left(\frac{1-p_{S|I,1}}{1-p_{\mathrm{H0}}}\right), \tag{D8}$$

$$C_2 = \ln\left(\frac{1-p_{S|I,0}}{1-p_{\mathrm{H0}}}\right). \tag{D9}$$

APPENDIX E: CLICK TO LLV DISTRIBUTION

The condition that the Gaussian regime is valid ensures that all click-count distributions can easily be transformed into its LLV form. This ease is afforded by the LLV for CI Eq. (D4) and QI Eq. (D5) being linear, this property preserves normality. The first two statistical moments of any click-count distribution are transformed such that the first two statistical moments are yielded for the LLV distributions. The following analysis is presented for the object present case. Deriving for the object absent case instead requires replacing the relevant click probabilities. Shown below is the transformation for the mean $\mu_{\mathrm{H1:CI}} = Np_{\mathrm{H1}}$ and standard deviation $\sigma_{\mathrm{H1:CI}} = \sqrt{Np_{\mathrm{H1}}(1-p_{\mathrm{H1}})}$ for CI

$$\mu_{\mathrm{H1:CI:\Lambda}} = \Lambda(\mu_{\mathrm{H1:CI}}, N), \tag{E1}$$

$$= M\mu_{\mathrm{H1:CI}} + NC \tag{E2}$$

and

$$\sigma_{\mathrm{H1:CI:\Lambda}} = M\sigma_{\mathrm{H1:CI}}. \tag{E3}$$

However, it is not as simple for QI. Equation (D5) encodes both coincidence clicks and noncoincidence click-count distributions into the one LLV distribution. Equation (D5) amounts to a linear combination, therefore normality is preserved for the resulting LLV distribution. If there has been k idler-click events, a click-count distribution's statistical moments $(\mu_{\mathrm{H1}:k}, \sigma_{\mathrm{H1}:k})$ are transformed into its respective LLV statistical moments as

$$\mu_{\mathrm{H1}:\Lambda(x,k)} = M_1 k p_{\mathrm{S|I,1}} + C_1 k + M_2\left((N-k)p_{S|I,0}\right) + \\ + (N-k)C_2 \tag{E4}$$

for the mean and

$$\sigma_{\mathrm{H1}:\Lambda(x,k)} = \left(M_1^2 k p_{S|I,1}(1-p_{S|I,1}) + \\ + M_2^2(N-k)p_{S|I,0}(1-p_{S|I,0})\right)^{0.5} \tag{E5}$$

for the standard deviation. Much of the characterization of system performance is oriented around the LLV distributions after mean idler clicks $\mu_I = Np_I$, rather than for k idler clicks. Therefore, the mean of the object present LLV distribution after mean idler clicks is defined as

$$\mu_{\mathrm{H1}:\Lambda(x,\mu_I)} = N\big(p_I(M_1 p_{S|I,1} + C_1 - M_2 p_{S|I,0} - C_2) + \\ + M_2 p_{S|I,0} + C_2\big). \tag{E6}$$

The standard deviation of the object present LLV distribution after mean idler clicks is

$$\sigma_{\mathrm{H1}:\Lambda(x,\mu_I)} = \big(N\big(p_I(M_1^2 p_{S|I,1}(1 - p_{S|I,1}) + \\ - M_2^2 p_{S|I,0}(1 - p_{S|I,0})) + \\ + M_2^2 p_{S|I,0}(1 - p_{S|I,0})\big)\big)^{0.5}. \tag{E7}$$

APPENDIX F: FOM COMPARISON

The FOMs, distinguishability ϕ, SNR, and CRLB for signal loss estimation, when compared illustrates why the distinguishability ϕ is suitable in the detection-decision orientated theory. Comparing performance of QI and CI as a ratio of their respective distinguishabilities in certain regimes is vulnerable to the issues of divergence ($\phi_{\mathrm{t:CI}} = 0$) or saturation ($\phi_{\mathrm{t:QI,CI}} = 1$). Instead, the ratio of the QI and CI shots required N_{t} for a distinguishability ϕ is used in this paper. Shots required for threshold distinguishability N_{t} frames performance as a ratio of time required for confident detection, which is intuitive. Regardless, comparing the values of the QI and CI distinguishabilities still functions as a method of comparing system performance.

The SNR can yield the same result for multiple different regimes, hence it has no uniqueness, therefore it is insufficient for characterizing detection-decision performance.

Moreover, the CRLB for signal attenuation estimation, while well grounded in estimation theory and developed for the context of quantum illumination photocounting in Ref. [51], it does not directly instruct whether a confident decision can be made or not.

This Appendix focuses on QI for the FOMs, as it is straightforward to apply these approaches to CI. The SNR is defined as

$$\mathrm{SNR} = \frac{N_{\mathrm{coincidences}}}{N_{\mathrm{noise}}}, \tag{F1}$$

where $N_{\mathrm{coincidences}}$ is the number of coincidence clicks (without noise in the system) and N_{noise} is the number of coincidence clicks from noise (when the pump beam is switched off). Signal attenuation is estimated with ξ. The following analysis can proceed assuming that the signal attenuation estimation is greater than the uncertainty of the signal attenuation estimation. The CRLB instructs system performance by stating how easy an object's presence can be discerned, subject to noise and the variance of the underlying distribution. It is defined, for an estimator of signal attenuation $\hat{\xi}$, that the CRLB is

$$\Delta^2\hat{\xi} = \mathbb{E}\left(\frac{-\partial^2 \ln P_{\mathrm{H1}}(\xi)}{\partial(\xi)^2}\right)^{-1}. \tag{F2}$$

Following from this, the FOM is given with respect to the estimated signal attenuation and in decibels as

$$\Delta^2\hat{\xi}\ (\mathrm{dB}) = 10\log_{10}\left(\frac{\Delta^2\hat{\xi}}{\hat{\xi}}\right). \tag{F3}$$

APPENDIX G: DISTINGUISHABILITY DISCREPANCY

The LLV after k idler clicks processes coincidence (and possibly noncoincidence) click data, which has had k idler clicks, once this processing has occurred the knowledge of the underlying click data is obscured and only a LLV is known. Neglecting our knowledge of how many idler clicks there has been simplifies the postprocessing of LLV data. Therefore, for any LLV after k idler clicks this LLV can be processed with any other LLV with $\tilde{k} \neq k$ idler clicks. In other words, each LLV after any number of idler clicks are equivalent to each other in postprocessing. Hence, the discrepancy in the effectiveness of each LLV test after k idler clicks is limited is key. Otherwise this equivalency is erroneous.

Given a single regime, QI has object present and absent LLV distributions for each k idler clicks. This corresponds to a distinguishability for each LLV after k idler clicks, which is denoted as ϕ_k. The system performance is characterized in terms of the threshold distinguishability ϕ_{t}, which is calculated from the LLV distributions after mean idler clicks. Consequently, there must be only a limited discrepancy between any ϕ_k and ϕ_{t}, for LLV equivalency to be valid.

Bounds are placed on what is considered to be extremal numbers of k idler clicks. With the minimum and maximum k idler clicks being set as $I_{\min} = \lfloor(\mu_I - 4\sigma_I)\rfloor$ and $I_{\max} = \lfloor(\mu_I + 4\sigma_I)\rfloor$, respectively. With μ_I as the mean and σ_I as the standard deviation of the idler-click distribution.

The condition for limited discrepancy is arbitrarily set as $T_\phi = 0.05$. Therefore, a regime has an acceptable amount of distinguishability discrepancy if both criterion

$$\frac{|\phi_{\mathrm{t}} - \phi_{I_{\min}}|}{\phi_{\mathrm{t}}} \leq T_\phi \quad \text{and} \quad \frac{|\phi_{\mathrm{t}} - \phi_{I_{\max}}|}{\phi_{\mathrm{t}}} \leq T_\phi \tag{G1}$$

are satisfied.

APPENDIX H: SOLVING DISTINGUISHABILITY EQUATION

The distinguishability measure for the LLV distributions after mean idler clicks is defined as

$$\phi = 1 - \big((1 - Q(0, \mu_{\mathrm{H1}:\Lambda(x,\mu_I)}, \sigma_{\mathrm{H1}:\Lambda(x,\mu_I)})) + \\ + Q(0, \mu_{\mathrm{H0}:\Lambda(x,\mu_I)}, \sigma_{\mathrm{H0}:\Lambda(x,\mu_I)})\big), \tag{H1}$$

where $Q(d_{\mathrm{LLV}}, \mu, \sigma)$ is the Gaussian Q function. The statistical moments $\mu_{\Lambda(x,\mu_I)}$ and $\sigma_{\Lambda(x,\mu_I)}$ are from the LLV distributions for object present or absent. The Gaussian Q function can be approximated by the error function $\mathrm{Erf}(d_{\mathrm{LLV}})$ as

$$Q(d_{\mathrm{LLV}}, \mu, \sigma) = 0.5\left(1 - \mathrm{Erf}\left(\frac{d_{\mathrm{LLV}} - \mu}{\sigma\sqrt{2}}\right)\right). \tag{H2}$$

Hence, the definition of ϕ is restated as

$$\phi = 0.5\left(\mathrm{Erf}\left(\frac{-\mu_{\mathrm{H0}:\Lambda}}{\sigma_{\mathrm{H0}:\Lambda}\sqrt{2}}\right) + \mathrm{Erf}\left(\frac{\mu_{\mathrm{H1}:\Lambda}}{\sigma_{\mathrm{H1}:\Lambda}\sqrt{2}}\right)\right). \tag{H3}$$

The signage for above is dictated by the need for a positive argument in the error function. Solving Eq. (H3) to find the parameters required for $\phi = \phi_{\mathrm{t}}$ needs the shots required for threshold distinguishability N_{t} to be found. Firstly, for QI the shots required is decomposed into $N_{\mathrm{t}} = N_{I1} + N_{I0}$ and $N_{\mathrm{t}} = (N_{I1}/p_I)$, where N_{I1} and N_{I0} are shots when the idler does and does not fire, respectively. From the prior definitions it is clear that $N_{I0} = N_{I1}((1/(p_I)) - 1)$. Equation (H3) framed in terms of the variable N_{I1} when $\phi = \phi_{\mathrm{t}}$ is expressed as

$$\phi_{\mathrm{t}} = 0.5\left(\mathrm{Erf}(-G_0\sqrt{N_{I1}}) + \mathrm{Erf}(G_1\sqrt{N_{I1}})\right), \tag{H4}$$

where

$$G = \frac{M_1 p_{I1} + C_1 + \left(\frac{1}{p_I} - 1\right)(M_2 p_{I0} + C_2)}{\sqrt{2}\left(M_1^2 p_{I1}(1 - p_{I1}) + M_2^2\left(\frac{1}{p_I} - 1\right) p_{I0}(1 - p_{I0})\right)^{0.5}}.$$

Replacing object present and absent click probabilities to yield G_1 and G_0, respectively. Therefore, N_{I1} is numerically solved with the inverse function of ϕ_{t}

$$N_{I1} = \mathrm{F}^{-1}(\phi_{\mathrm{t}}). \tag{H5}$$

Following this, the shots required for threshold distinguishability is

$$N_{\mathrm{t}} = \left\lfloor \left(\frac{N_{I1}}{p_I}\right) \right\rfloor. \tag{H6}$$

[1] S. Lloyd, Enhanced sensitivity of photodetection via quantum illumination, Science **321**, 1463 (2008).

[2] S. H. Tan, B. I. Erkmen, V. Giovannetti, S. Guha, S. Lloyd, L. Maccone, S. Pirandola, and J. H. Shapiro, Quantum illumination with Gaussian states, Phys. Rev. Lett. **101**, 253601 (2008).

[3] S. Guha and B. I. Erkmen, Gaussian-state quantum-illumination receivers for target detection, Phys. Rev. A **80**, 052310 (2009).

[4] Z. Zhang, M. Tengner, T. Zhong, F. N. C. Wong, and J. H. Shapiro, Entanglement's benefit survives an entanglement-breaking channel, Phys. Rev. Lett. **111**, 010501 (2013).

[5] S. Zhang, X. Zou, J. Shi, J. Guo, and G. Guo, Quantum illumination in the presence of photon loss, Phys. Rev. A **90**, 052308 (2014).

[6] Z. Zhang, S. Mouradian, F. N. C. Wong, and J. H. Shapiro, Entanglement-enhanced sensing in a lossy and noisy environment, Phys. Rev. Lett. **114**, 110506 (2015).

[7] S. Barzanjeh, S. Guha, C. Weedbrook, D. Vitali, J. H. Shapiro, and S. Pirandola, Microwave quantum illumination, Phys. Rev. Lett. **114**, 080503 (2015).

[8] C. Weedbrook, S. Pirandola, J. Thompson, V. Vedral, and M. Gu, How discord underlies the noise resilience of quantum illumination, New J. Phys. **18**, 43027 (2016).

[9] Q. Zhuang, Z. Zhang, and J. H. Shapiro, Entanglement-enhanced Neyman-Pearson target detection using quantum illumination, J. Opt. Soc. Am. B **34**, 1567 (2017).

[10] Q. Zhuang, Z. Zhang, and J. H. Shapiro, Optimum mixed-state discrimination for noisy entanglement-enhanced sensing, Phys. Rev. Lett. **118**, 040801 (2017).

[11] Q. Zhuang, Z. Zhang, and J. H. Shapiro, Quantum illumination for enhanced detection of Rayleigh-fading targets, Phys. Rev. A **96**, 20302 (2017).

[12] B. Xiong, X. Li, X.-Y. Wang, and L. Zhou, Improve microwave quantum illumination via optical parametric amplifier, Ann. Phys.-New York **385**, 757 (2017).

[13] S. Pirandola, B. R. Bardhan, T. Gehring, C. Weedbrook, and S. Lloyd, Advances in photonic quantum sensing, Nat. Photonics **12**, 724 (2018).

[14] R. Nair and M. Gu, Fundamental limits of quantum illumination, Optica **7**, 771 (2020).

[15] A. Karsa and S. Pirandola, Noisy receivers for quantum illumination, IEEE Aerosp. Electron. Syst. Mag. **35**, 22 (2020).

[16] A. Karsa, G. Spedalieri, Q. Zhuang, and S. Pirandola, Quantum illumination with a generic Gaussian source, Phys. Rev. Res. **2**, 023414 (2020).

[17] M.-H. Yung, F. Meng, X.-M. Zhang, and M.-J. Zhao, One-shot detection limits of quantum illumination with discrete signals, npj Quantum Inf. **6**, 75 (2020).

[18] Y. Jo, S. Lee, Y. S. Ihn, Z. Kim, and S.-Y. Lee, Quantum illumination receiver using double homodyne detection, Phys. Rev. Res. **3**, 013006 (2021).

[19] X. Chen and Q. Zhuang, Entanglement-assisted detection of fading targets via correlation-to-displacement conversion, Phys. Rev. A **107**, 62405 (2023).

[20] R. Wei, J. Li, W. Wang, S. Meng, B. Zhang, and Q. Guo, Comparison of SNR gain between quantum illumination radar and classical radar, Opt. Express **30**, 36167 (2022).

[21] G. Sorelli, N. Treps, F. Grosshans, and F. Boust, Detecting a target with quantum entanglement, IEEE Aerosp. Electron. Syst. Mag. **37**, 68 (2022).

[22] S. Borderieux, A. Coatanhay, and A. Khenchaf, Estimation of the influence of a noisy environment on the binary decision strategy in a quantum illumination radar, Sensors **22**, 4821 (2022).

[23] J. H. Shapiro and S. Lloyd, Quantum illumination versus coherent-state target detection, New J. Phys. **11**, 63045 (2009).

[24] A. R. U. Devi and A. K. Rajagopal, Quantum target detection using entangled photons, Phys. Rev. A **79**, 062320 (2009).

[25] S. M. Barnett and S. Croke, Quantum state discrimination, Adv. Opt. Photonics **1**, 238 (2009).

[26] M. F. Sacchi, Entanglement can enhance the distinguishability of entanglement-breaking channels, Phys. Rev. A **72**, 014305 (2005).

[27] C. W. S. Chang, A. M. Vadiraj, J. Bourassa, B. Balaji, and C. M. Wilson, Quantum-enhanced noise radar, Appl. Phys. Lett. **114**, 112601 (2019).

[28] S. Barzanjeh, S. Pirandola, D. Vitali, and J. M. Fink, Microwave quantum illumination using a digital receiver, Sci. Adv. **6**, eabb0451 (2020).

[29] D. Luong, C. W. S. Chang, A. M. Vadiraj, A. Damini, C. M. Wilson, and B. Balaji, Receiver operating characteristics for a prototype quantum two-mode squeezing radar, IEEE Trans. Aerosp. Electron. Syst. **56**, 2041 (2020).

[30] H. Shi, B. Zhang, and Q. Zhuang, Fulfilling entanglement's optimal advantage via converting correlation to coherence, ArXiv:quant-ph/2207.06609.

[31] H. Shi, B. Zhang, J. H. Shapiro, Z. Zhang, and Q. Zhuang, Optimal entanglement-assisted electromagnetic sensing and communication in the presence of noise, ArXiv:quant-ph/2309.12629.

[32] M. Reichert, Q. Zhuang, J. H. Shapiro, and R. Di Candia, Quantum illumination with a hetero-homodyne receiver and sequential detection, Phys. Rev. Appl. **20**, 14030 (2023).

[33] E. D. Lopaeva, I. Ruo Berchera, I. P. Degiovanni, S. Olivares, G. Brida, and M. Genovese, Experimental realization of quantum illumination, Phys. Rev. Lett. **110**, 153603 (2013).

[34] S. Ragy, I. Ruo Berchera, I. P. Degiovanni, S. Olivares, M. G. A. Paris, G. Adesso, and M. Genovese, Quantifying the source of enhancement in experimental continuous variable quantum illumination, J. Opt. Soc. Am. B **31**, 2045 (2014).

[35] A. Meda, E. Losero, N. Samantaray, F. Scafirimuto, S. Pradyumna, A. Avella, I. Ruo Berchera, and M. Genovese, Photon-number correlation for quantum enhanced imaging and sensing, J. Opt. (U. K.) **19**, 94002 (2017).

[36] T. Gregory, P.-A. Moreau, E. Toninelli, and M. J. Padgett, Imaging through noise with quantum illumination, Sci. Adv. **6**, eaay2652 (2020).

[37] G. Ortolano, E. Losero, S. Pirandola, M. Genovese, and I. Ruo Berchera, Experimental quantum reading with photon counting, Sci. Adv. **7**, eabc7796 (2023).

[38] J. Zhao, A. Lyons, A. C. Ulku, H. Defienne, D. Faccio, and E. Charbon, Light detection and ranging with entangled photons, Opt. Express **30**, 3675 (2022).

[39] P. S. Blakey, H. Liu, G. Papangelakis, Y. Zhang, Z. M. Léger, M. L. Iu, and A. S. Helmy, Quantum and non-local effects offer over 40 db noise resilience advantage towards quantum lidar, Nat. Commun. **13**, 5633 (2022).

[40] J. D. Franson, Nonlocal cancellation of dispersion, Phys. Rev. A **45**, 3126 (1992).

[41] D. G. England, B. Balaji, and B. J. Sussman, Quantum-enhanced standoff detection using correlated photon pairs, Phys. Rev. A **99**, 023828 (2019).

[42] H. Yang, W. Roga, J. Pritchard, and J. Jeffers, in *Proc. SPIE* (SPIE, Strasbourg, 2020), Vol. 11347, p. 113470I.

[43] H. He, D. Giovannini, H. Liu, E. Chen, Z. Yan, and A. S. Helmy, Non-classical semiconductor photon sources enhancing the performance of classical target detection systems, J. Light. Technol. **38**, 4540 (2020).

[44] H. Liu, B. Balaji, and A. S. Helmy, Target detection aided by quantum temporal correlations: Theoretical analysis and experimental validation, IEEE Trans. Aerosp. Electron. Syst. **56**, 3529 (2020).

[45] H. Yang, W. Roga, J. D. Pritchard, and J. Jeffers, Gaussian state-based quantum illumination with simple photodetection, Opt. Express **29**, 8199 (2021).

[46] R. J. Murchie, J. D. Pritchard, and J. Jeffers, in *Proc. SPIE* (SPIE, San Diego, 2021), Vol. 11835, p. 118350G.

[47] H. Yang, N. Samantaray, and J. Jeffers, Quantum illumination with multiplexed photodetection, Phys. Rev. Appl. **18**, 034021 (2022).

[48] Q. Zhuang, Z. Zhang, and J. H. Shapiro, Entanglement-enhanced lidars for simultaneous range and velocity measurements, Phys. Rev. A **96**, 40304 (2017).

[49] M. Reichert, R. Di Candia, M. Z. Win, and M. Sanz, Quantum-enhanced Doppler lidar, npj Quantum Inf. **8**, 147 (2022).

[50] C. W. Helstrom, Quantum detection and estimation theory, J. Stat. Phys. **1**, 231 (1969).

[51] H. Liu, D. Giovannini, H. He, D. England, B. J. Sussman, B. Balaji, and A. S. Helmy, Enhancing lidar performance metrics using continuous-wave photon-pair sources, Optica **6**, 1349 (2019).

[52] S. Frick, A. McMillan, and J. Rarity, Quantum rangefinding, Opt. Express **28**, 37118 (2020).

[53] Q. Zhuang, Quantum ranging with Gaussian entanglement, Phys. Rev. Lett. **126**, 240501 (2021).

[54] H. Kuniyil, H. Ozel, H. Yilmaz, and K. Durak, Noise-tolerant object detection and ranging using quantum correlations, J. Opt. (U. K.) **24**, 105201 (2022).

[55] M. P. Mrozowski, R. J. Murchie, J. Jeffers, and J. D. Pritchard, Demonstration of quantum-enhanced rangefinding robust against classical jamming, Opt. Express **32**, 2916 (2024).

[56] C. M. Caves and B. L. Schumaker, New formalism for two-photon quantum optics. I. Quadrature phases and squeezed states, Phys. Rev. A **31**, 3068 (1985).

[57] S. M. Barnett and P. L. Knight, Squeezing in correlated quantum systems, J. Mod. Opt. **34**, 841 (1987).

[58] D. Renker, Geiger-mode avalanche photodiodes, history, properties and problems, Nucl. Instrum. **567**, 48 (2006).

[59] S. M. Barnett, L. S. Phillips, and D. T. Pegg, Imperfect photodetection as projection onto mixed states, Opt. Commun. **158**, 45 (1998).

[60] P. P. Rohde and T. C. Ralph, Modelling photo-detectors in quantum optics, J. Mod. Opt. **53**, 1589 (2006).
[61] L. Mandel and E. Wolf, *Optical Coherence and Quantum Optics* (Cambridge University Press, Cambridge, 1995).
[62] S. Barnett and P. M. Radmore, *Methods in Theoretical Quantum Optics* (Oxford Academic, Oxford, 2002).
[63] S. M. Barnett, *Quantum Information* (Oxford University Press, Oxford, 2009).
[64] M. Wilde, *Quantum Information Theory* (Cambridge University Press, Cambridge, 2013).
[65] G. Spedalieri and S. L. Braunstein, Asymmetric quantum hypothesis testing with Gaussian states, Phys. Rev. A **90**, 052307 (2014).
[66] M. M. Wilde, M. Tomamichel, S. Lloyd, and M. Berta, Gaussian hypothesis testing and quantum illumination, Phys. Rev. Lett. **119**, 120501 (2017).
[67] Q. Zhuang and S. Pirandola, Entanglement-enhanced testing of multiple quantum hypotheses, Commun. Phys. **3**, 103 (2020).
[68] A. Papoulis and S. Pillai, *Probability, Random Variables, and Stochastic Processes* (McGraw-Hill, New York, 1984), p. 57.
[69] P. H. Garthwaite, I. T. Jolliffe, and B. Jones, *Statistical Inference* (Oxford University Press, Oxford, 2002).
[70] J. Neyman and E. S. Pearson, On the problem of the most efficient tests of statistical hypotheses, Philos. Trans. R. Soc. London. Ser. A **231**, 0289 (1933).
[71] J. K. Ghosh, Only linear transformations preserve normality, Sankhyā: Indian J. Stat. **31**, 309 (1969).
[72] A. Chefles, Quantum state discrimination, Contemp. Phys. **41**, 0401 (2000).
[73] R. Nair and M. Gu, Quantum sensing of phase-covariant optical channels, ArXiv:quant-ph/2306.15256.
[74] D. Petz and C. Ghinea, *QP-PQ: Quantum Probability and White Noise Analysis*, edited by R. Rebolledo (World Scientific, New Jersey, 2011), Vol. 27, pp. 261–281.
[75] L. Cohen, E. S. Matekole, Y. Sher, D. Istrati, H. S. Eisenberg, and J. P. Dowling, Thresholded quantum lidar: Exploiting photon-number-resolving detection, Phys. Rev. Lett. **123**, 203601 (2019).
[76] S. J. Koppal, *Computer Vision: A Reference Guide* (Springer, New York, 2014).
[77] S. Frick, Quantum rangefinding, Ph.D. thesis, University of Bristol, 2019.
[78] R. J. Murchie, J. D. Pritchard, and J. Jeffers, Data for "Object detection and range finding with quantum states using simple detection" (University of Strathclyde, 2024).
[79] E. C. G. Sudarshan, Equivalence of semiclassical and quantum mechanical descriptions of statistical light beams, Phys. Rev. Lett. **10**, 277 (1963).
[80] D. B. Horoshko, S. De Bièvre, G. Patera, and M. I. Kolobov, Thermal-difference states of light: Quantum states of heralded photons, Phys. Rev. A **100**, 053831 (2019).